

Article

Geochemistry, Chronology and Tectonic Implications of the Hadayang Schists in the Northern Great Xing'an Range, Northeast China

Fuchao Na, Weimin Song *, Yingcai Liu, Junyu Fu, Yan Wang and Wei Sun

Shenyang Center of China Geological Survey, Shenyang 110034, China; nafuchao@mail.cgs.gov.cn (F.N.); sylyingcai@126.com (Y.L.); fjyzyx@163.com (J.F.); wy68413@163.com (Y.W.); soohiboy@126.com (W.S.)

* Correspondence: swmws@126.com

Abstract: The Late Paleozoic tectonic evolution of the Xing'an block in the eastern Central Asian orogenic belt has long been the subject of debate. In this paper, a comprehensive study of U-Pb zircon ages, Lu-Hf isotopes and whole-rock elemental analyses was carried out on Hadayang schists. Representative samples of the epidote-biotite-albite schist and biotite-albite schist yielded the weighted mean $^{206}\text{Pb}/^{238}\text{U}$ ages of 360 ± 2 Ma and 355 ± 3 Ma, respectively. This indicated the presence of Late Devonian–Early Carboniferous intermediate-basic rocks in the eastern Xing'an block. The Hadayang schists exhibited a Na-rich, tholeiitic and calc-alkaline affinity in composition with low Mg# (35.2–53.0), Cr (23.7–86.5 ppm), Ni (21.1–40.0 ppm) and Co (12.1–30.6 ppm). They were characterized by enrichment of LILEs, depletion of HFSEs and highly positive zircon $\varepsilon_{\text{Hf}}(t)$ values (the average values were +8.93 and +9.29, respectively). The magma source of the Hadayang schists was a mantle that consisted of both spinel and garnet lherzolite, with a partial melting degree of 1%–5%, and it had undergone fractional crystallization of olivine, orthopyroxene and plagioclase. The Hadayang schists, together with other Late Devonian–Early Carboniferous intermediate-basic magmatic rocks in the eastern Xing'an block, were formed in an intracontinental extension tectonic setting similar to that of the North American Basin and Range basalt. Moreover, Late Devonian–Early Carboniferous ophiolite under a similar tectonic background in the western Xing'an block has been reported. We believe that the Xing'an block would have been in the stage of intracontinental extension during the Late Devonian–Early Carboniferous.

Keywords: eastern Xing'an block; late Devonian–early Carboniferous; Hadayang schists; petrogenesis; tectonic implications



Citation: Na, F.; Song, W.; Liu, Y.; Fu, J.; Wang, Y.; Sun, W. Geochemistry, Chronology and Tectonic Implications of the Hadayang Schists in the Northern Great Xing'an Range, Northeast China. *Minerals* **2023**, *13*, 1379. <https://doi.org/10.3390/min13111379>

Academic Editor: Manuel Francisco Pereira

Received: 14 August 2023

Revised: 23 October 2023

Accepted: 25 October 2023

Published: 28 October 2023



Copyright: © 2023 by the authors. Licensee MDPI, Basel, Switzerland. This article is an open access article distributed under the terms and conditions of the Creative Commons Attribution (CC BY) license (<https://creativecommons.org/licenses/by/4.0/>).

1. Introduction

The Central Asian orogenic belt (CAOB) is located between the Siberian craton and the Sino-Korean craton, and is composed of a series of micro-continental blocks and suture zones [1–5] (Figure 1a). The Xing'an–Mongolia orogenic belt (XMOB) is located in the eastern section of the CAOB, and is made up of several microcontinents, including the Erguna, Xing'an, Songnen and Jiamusi–Khanka blocks [6–11] (Figure 1b). Although much progress has been made in the study area of the tectonic pattern and evolutionary history of the XMOB in recent years, there are still many controversies, among which the dating of the integration of the Xing'an (XB) and Songnen blocks (SB) is the most prominent. For example, Xu et al. [6] argued that the XB and SB combined along the Angin Sum–Xilinhot–Heihe line before the Devonian [7,12]; Liu et al. [8] proposed that these two blocks closed along the Hegenshan–Moguqi–Heihe line during the late Early Carboniferous and early Late Carboniferous [9,13–15]; Xu et al. [11] believed that the XB and SB combined along the Xilinhot–Ulanhot–Nenjiang–Heihe line, and the time limit was the late Early Carboniferous [16]. In addition, the time limit of convergence is also dated

to the Late Devonian to Early Carboniferous [17,18], to before the Permian [19,20] and to the Triassic [21,22].

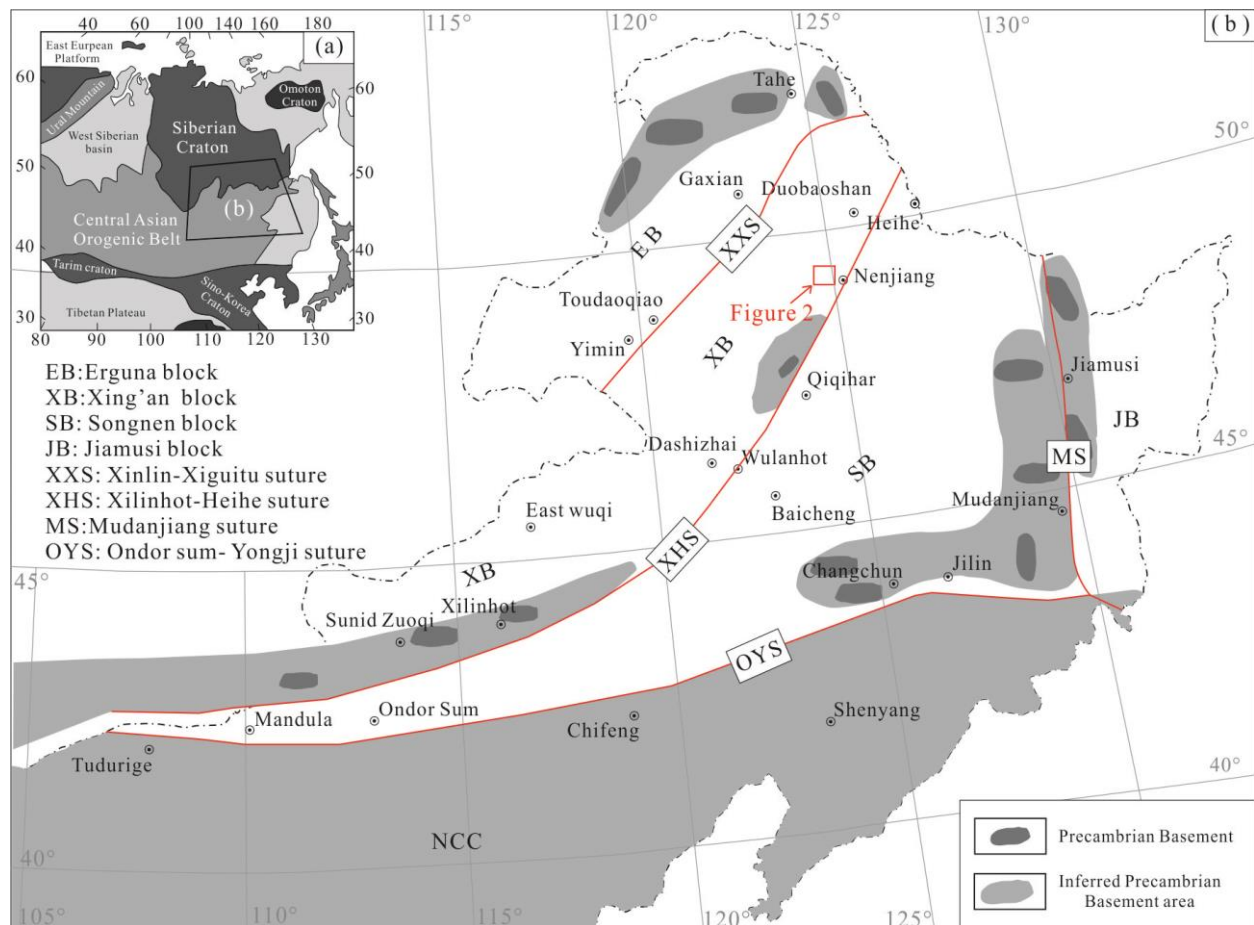


Figure 1. Pre-Devonian blocks in XMOB, northeast China: (a) location of the CAOB; (b) blocks in the XMOB (modified after [7]).

Through the analysis of the above different views, it can be found that one of the focuses of the debate is whether there was subduction in the ocean basin between the XB and the SB in the late Paleozoic, and the study of the tectonic background of the late Paleozoic igneous rock in the XB can provide important evidence for solving the above problems. Compared with granitic rocks, mafic magmatic rocks originate directly from partial melting of mantle and the geochemistry is less affected by late transformation, so they become ideal objects for the derivation of mantle source characteristics and regional tectonic background [23]. Therefore, we report zircon U-Pb geochronology, Hf isotopes and whole-rock geochemistry studies on late Devonian–early Carboniferous metamorphic intermediate-basic volcanic rocks in the southern XB, to determine their origins and tectonic setting. This study provides a more detailed understanding of the evolution history of the XB and SB in the late Paleozoic. Furthermore, it provides important constraints for the study of the tectonic evolution of the XMOB.

2. Geological Settings and Sampling

The study area was located in the Hadayang area of Molidawa Banner in the eastern part of the Inner Mongolia Autonomous Region and it tectonically belongs to the southern part of the XB (Figure 2). As the oldest block in the XMOB, the Precambrian record of the EB is well developed, and the oldest rock exposed is a set of Neoproterozoic–Paleoproterozoic granitic gneiss [24–27]. The Xinghuadukou Group, which was previously considered to be of Paleo–Mesoproterozoic age, may have formed in the Neoproterozoic [27–31].

In addition, Neoproterozoic magmatism is also well developed in the EB [31–34]. The XB is traditionally based on Precambrian strata such as the Xinghuadukou Group, the Jiageda Formation and the Wolegen Group, but recent research shows that these strata were formed in the Paleozoic [35–37]. In recent years, a series of Neoarchean–Paleoproterozoic magmatic rocks [38–42] and metamorphic rock series [43] have been identified in the Ulanhot–Longjiang area, suggesting the existence of Precambrian basement in the XB. After the convergence of the EB and XB along the XXS in the early Paleozoic [44–49] (Figure 1b), the Erguna–Xing’an block (EXB) was covered by the Early Paleozoic–Lower Permian marine and continental alternative deposition, the Upper Permian continental sedimentary strata and the Mesozoic volcanoclastic rocks, and developed multistage Paleozoic–Mesozoic magmatic intrusion. The SB is located in the southeast of the EXB, which is bounded by the XHS (Figure 1b). The Dongfengshan Group and Tadong Group in the eastern SB, which are traditionally considered as “Paleoproterozoic”, were formed in the Neoproterozoic [50–52], accompanied by contemporaneous magmatic intrusions [53–56]. The western SB is mostly covered by late Mesozoic–Cenozoic volcanoclastic sediments.

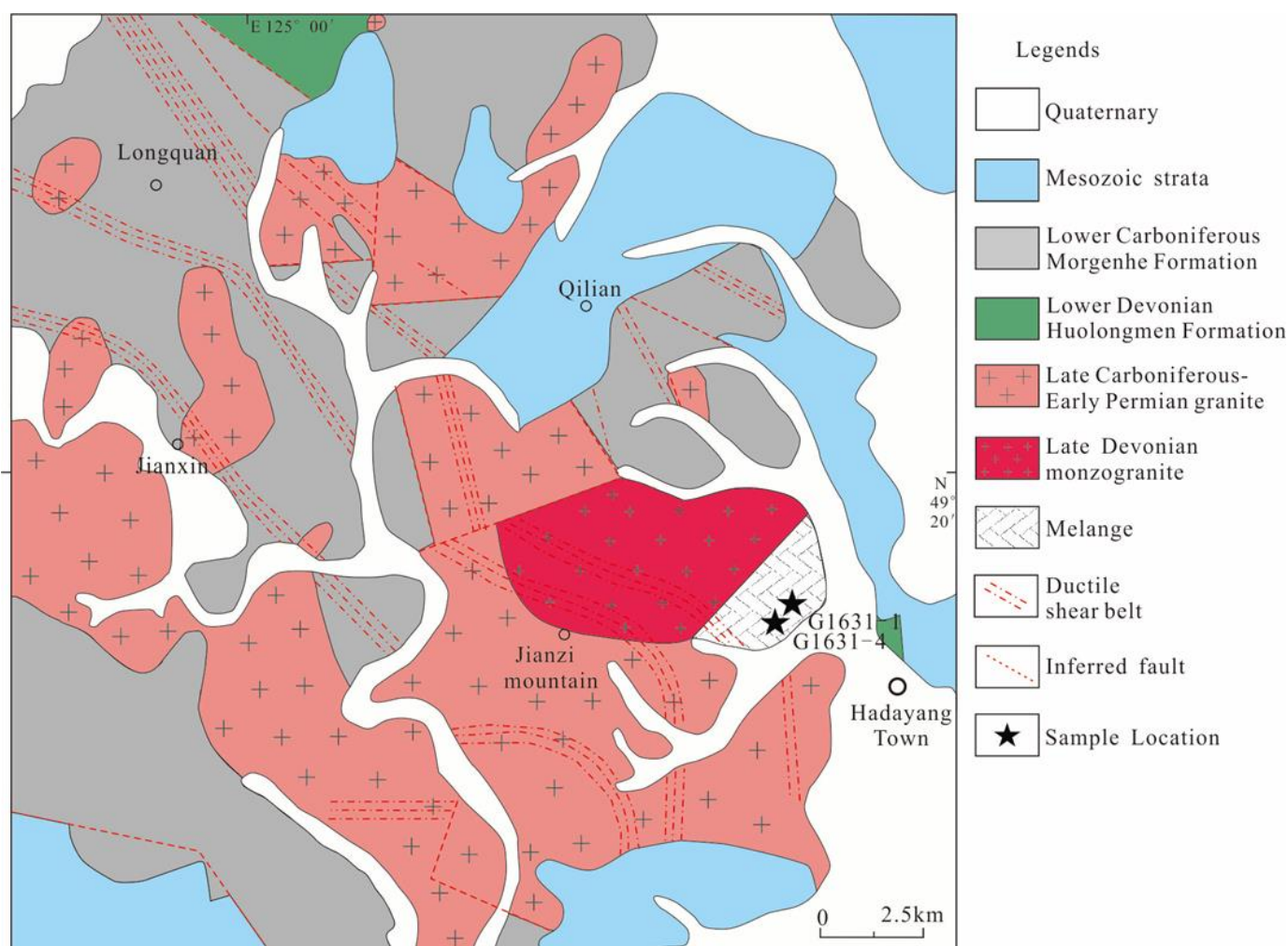


Figure 2. Simplified geological map of Hadayang area and locations of samples used in this study.

The late Paleozoic strata in the study area include the Lower Devonian Huolongmen Formation and the Lower Carboniferous Morgenhe Formation (Figure 2). The Lower Devonian Huolongmen Formation is mainly composed of clastic sedimentary rocks with a small amount of intermediate volcanic rocks, and is affected by a poorly developed ductile deformation. The formation age of chlorite muscovite schist (protolith is volcanic rock) is 414 Ma [57]. The Lower Carboniferous Morgenhe Formation is mainly composed of

weakly metamorphic intermediate-acid volcanic rocks, which are generally mylonitic. The zircon U-Pb age of the volcanic rocks is 353 to 352 Ma [58,59]. Late Paleozoic intrusive rocks include Late Devonian mylonitic syenite granite [60], Late Carboniferous–Early Permian granodiorite, syenogranite and alkali feldspar granite. The above are mostly covered by Mesozoic volcanic rocks and Cenozoic detrital sedimentary rocks. In addition to the above features, there is also a Hadayang melange developed in the study area [61,62]. The matrix in the melange is mainly composed of schist, while blocks consist of schist, mafic–ultramafic rocks and meta-acidic volcanic rocks [62].

Two samples were collected from the blocks of Hadayang melange for age dating, and the sample locations are shown in Figure 2. At each of these two sites, six additional dating samples were collected for geochemical and petrological analysis. Sample G1631-1, an epidote-biotite-albite schist ($49^{\circ}18'28''$ N, $125^{\circ}06'33''$ E, Figures 2 and 3a–b), showed porphyroblastic, lepidoblastic texture and schistose structure (Figure 3c). The mineral assemblage consisted of albite (~27%), biotite (~30%), chlorite (~8%), epidote (~20%), quartz (~8%) and opaque mineral (~7%) (Figure 3c). The content of the remaining phenocryst was about 5%, and the composition included opaque mineral aggregates and albite. The matrix included biotite, chlorite, epidote, quartz and albite. Sample G1631-4, a biotite-albite schist ($49^{\circ}18'25''$ N, $125^{\circ}06'31''$ E), was located near Sample G1631-1 (Figures 2 and 3d–e). Petrographically, the biotite-albite schist had porphyroblastic, lepidoblastic texture and schistose structure, consisting of biotite (~15%), chlorite (~8%), epidote (~12%), albite (~40%) and quartz (~25%) (Figure 3f). The crystalloblasts were composed of oligoclase and albite, and the oligoclase was semi-euhedral wide plate with matrix components interspersed, and content of less than 1%. The albite was granular and contained matrix minerals biotite, chlorite and epidote inclusions, accounting for about 5%. The matrix included biotite, chlorite, epidote, quartz and albite (Figure 3f).

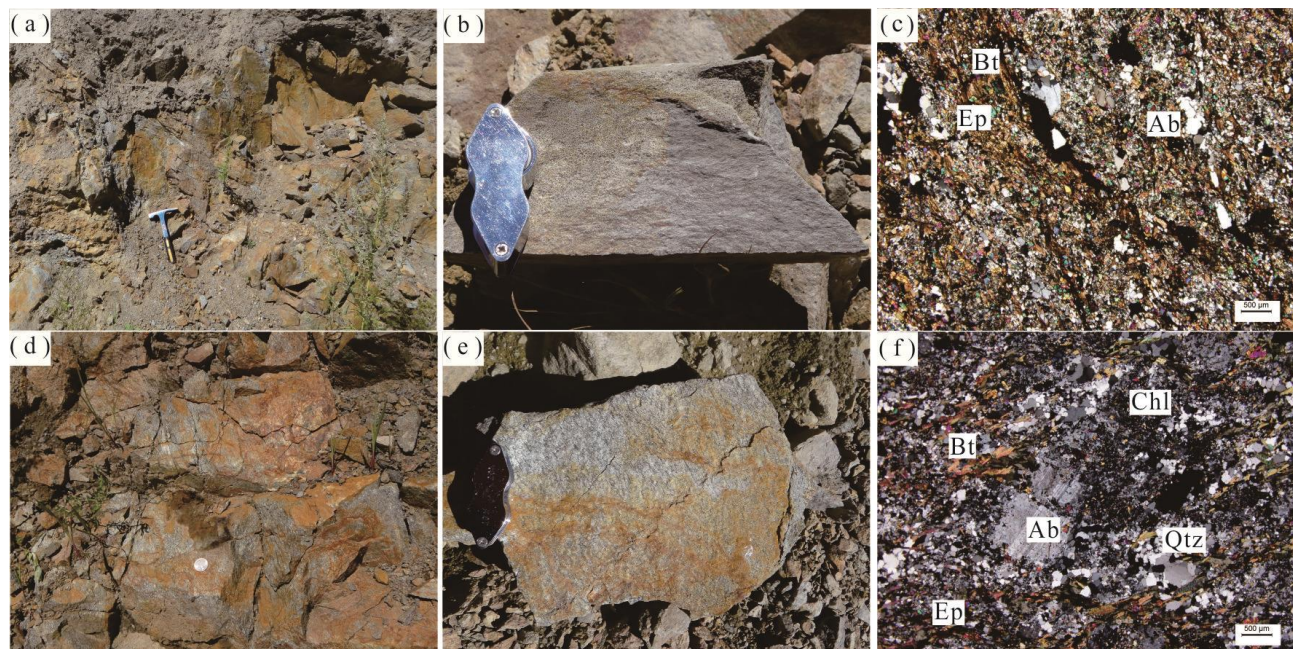


Figure 3. Field occurrence and microscope views of the Hadayang schists. (a–c) Epidote-biotite-albite schist. (d–f) Biotite-albite schist.

3. Analytical Methods

3.1. Major and Trace Element Analysis

The major and trace element analyses were carried out at the Shenyang Mineral Resources Supervision and Inspection Center, Shenyang, China. Whole-rock major element concentrations were determined by X-ray fluorescence spectrometry, yielding an analytical

precision better than 2%. Trace element and rare earth element (REE) concentrations were determined by ICP–MS, yielding an analytical precision better than 5% for elements with concentrations of >10 ppm, <8% for elements with concentrations of <10 ppm and <10% for the transition metals.

3.2. Zircon U–Pb Dating

U–Pb dating analyses were conducted by LA-ICP-MS at Beijing Createch Testing Technology Co., Ltd. (Beijing, China). The detailed operating conditions for the laser ablation system and the ICP-MS instrument and data reduction were the same as described by Hou et al. [63]. Laser sampling was performed using an ESI NWR 193 nm laser ablation system. An AnalytikJena PQMS Elite ICP-MS (Analytik Jena AG, Jena, Germany) instrument was used to acquire ion-signal intensities. Helium was applied as a carrier gas. Argon was used as the make-up gas and mixed with the carrier gas via a T-connector before entering the ICP. Each analysis incorporated a background acquisition of approximately 15–20 s (gas blank) followed by 45 s of data acquisition from the sample. Off-line raw data selection and integration of background and analyte signals, and time-drift correction and quantitative calibration for U–Pb dating, were performed by ICPMSDataCal [64]. Zircon GJ-1 was used as the external standard for U–Pb dating, and was analyzed twice every 5–10 analyses. Time-dependent drifts of U–Th–Pb isotopic ratios were corrected using a linear interpolation (with time) for every 5–10 analyses according to the variations of GJ-1 (i.e., 2 zircon GJ-1 + 5–10 samples + 2 zircon GJ-1) [64]. Uncertainty of preferred values for the external standard GJ-1 was propagated to the ultimate results of the samples. In all analyzed zircon grains, the common Pb correction was not necessary due to the low signal of common ^{204}Pb and high $^{206}\text{Pb}/^{204}\text{Pb}$. U, Th and Pb concentration was calibrated by NIST 610. Concordia diagrams and weighted mean calculations were made using IsoPlot/Ex_ver3. The zircon Plesovice was dated as unknown samples and yielded a weighted mean $^{206}\text{Pb}/^{238}\text{U}$ age of 337.5 ± 2.4 Ma (2SD, $n = 5$), which was in good agreement with the recommended $^{206}\text{Pb}/^{238}\text{U}$ age of 337.13 ± 0.37 Ma (2SD) [65].

3.3. Lu–Hf Isotope Analysis

Zircon in situ Hf isotope analysis was carried out using a RESOLUTION SE 193 laser-ablation system attached to a Thermo Fisher Scientific Neptune Plus MC-ICP-MS at Beijing Createch Testing Technology Co., Ltd (Beijing, China). Instrumental conditions and data acquisition protocols were as described by Hou et al. [66]. A stationary spot used a beam diameter of ~ 55 μm . Helium was used as the carrier gas to transport ablated material from the laser-ablation cell after which it was mixed with Ar prior to entering the ICP-MS torch. $^{176}\text{Lu}/^{175}\text{Lu} = 0.02658$ and $^{176}\text{Yb}/^{173}\text{Yb} = 0.796218$ ratios were determined to correct for the isobaric interferences of ^{176}Lu and ^{176}Yb on ^{176}Hf . For instrumental mass bias correction, Yb isotope ratios were normalized to $^{172}\text{Yb}/^{173}\text{Yb} = 1.35274$ and Hf isotope ratios to $^{179}\text{Hf}/^{177}\text{Hf} = 0.7325$ using an exponential law. The mass bias behavior of Lu was assumed to follow that of Yb; the mass bias correction protocol was as described by Hou et al. [66].

4. Analytical Results

4.1. Whole-Rock Geochemistry

Results of the major element, trace element and REE analyses of the samples from the Hadayang schists are listed in Table 1.

Table 1. Analytical results for the major (w%) and trace elements ($\times 10^{-6}$) of Hadayang schists.

| Lithology | Epidote-Biotite-Albite Schist | | | | | | Biotite-Albite Schist | | | | | |
|------------------------------------|-------------------------------|-----------|-----------|-----------|-----------|-----------|-----------------------|-----------|-----------|-----------|-----------|-----------|
| Sample No. | G1631-1.1 | G1631-1.2 | G1631-1.3 | G1631-1.4 | G1631-1.5 | G1631-1.6 | G1631-4.1 | G1631-4.2 | G1631-4.3 | G1631-4.4 | G1631-4.5 | G1631-4.6 |
| SiO ₂ (%) | 49.28 | 50.55 | 50.47 | 50.16 | 49.46 | 51.15 | 58.07 | 58.36 | 58.82 | 55.44 | 57.72 | 56.23 |
| Al ₂ O ₃ (%) | 16.75 | 16.56 | 16.76 | 16.51 | 16.99 | 16.73 | 15.98 | 15.84 | 16.17 | 16.46 | 16.27 | 16.30 |
| Fe ₂ O ₃ (%) | 8.08 | 7.80 | 7.18 | 7.97 | 7.95 | 7.61 | 2.97 | 2.73 | 2.65 | 2.89 | 5.57 | 5.18 |
| FeO (%) | 3.05 | 3.28 | 3.32 | 3.14 | 3.41 | 3.32 | 3.73 | 4.00 | 4.09 | 4.40 | 2.43 | 2.97 |
| CaO (%) | 12.68 | 11.54 | 9.51 | 11.27 | 12.09 | 11.42 | 4.43 | 4.93 | 4.24 | 5.30 | 5.93 | 6.97 |
| MgO (%) | 3.31 | 3.59 | 3.99 | 3.45 | 3.19 | 3.28 | 3.96 | 3.83 | 4.01 | 4.40 | 3.04 | 3.17 |
| K ₂ O (%) | 0.17 | 0.18 | 0.73 | 0.26 | 0.09 | 0.02 | 0.76 | 0.86 | 1.40 | 0.90 | 1.38 | 1.97 |
| Na ₂ O (%) | 0.32 | 0.42 | 1.28 | 0.47 | 0.26 | 0.03 | 4.82 | 3.86 | 4.33 | 3.97 | 2.77 | 2.68 |
| TiO ₂ (%) | 1.80 | 1.70 | 1.79 | 1.68 | 1.77 | 1.66 | 1.08 | 1.02 | 1.02 | 1.06 | 1.58 | 1.34 |
| P ₂ O ₅ (%) | 1.07 | 1.02 | 1.12 | 1.02 | 1.05 | 1.03 | 0.61 | 0.57 | 0.58 | 0.61 | 0.75 | 0.69 |
| MnO (%) | 0.14 | 0.15 | 0.13 | 0.15 | 0.16 | 0.15 | 0.18 | 0.17 | 0.13 | 0.19 | 0.13 | 0.15 |
| LOI (%) | 3.48 | 3.45 | 3.45 | 3.45 | 3.36 | 3.47 | 3.24 | 3.59 | 2.67 | 4.05 | 2.23 | 2.26 |
| SUM | 100.14 | 100.26 | 99.75 | 99.53 | 99.78 | 99.86 | 99.83 | 99.75 | 100.11 | 99.67 | 99.81 | 99.90 |
| FeO ^T | 10.33 | 10.29 | 9.79 | 10.32 | 10.57 | 10.18 | 6.40 | 6.45 | 6.47 | 7.01 | 7.44 | 7.63 |
| Mg# | 36.51 | 38.50 | 42.25 | 37.53 | 35.14 | 36.62 | 52.61 | 51.58 | 52.63 | 52.97 | 42.30 | 42.74 |
| Na ₂ O/K ₂ O | 1.96 | 2.31 | 1.76 | 1.84 | 2.98 | 1.56 | 6.35 | 4.47 | 3.08 | 4.43 | 2.01 | 1.36 |
| Na ₂ O+K ₂ O | 0.51 | 0.62 | 2.09 | 0.76 | 0.36 | 0.04 | 5.77 | 4.91 | 5.88 | 5.09 | 4.26 | 4.76 |
| σ | 0.03 | 0.04 | 0.46 | 0.06 | 0.02 | 0.00 | 1.95 | 1.37 | 1.99 | 1.73 | 1.12 | 1.55 |
| Y | 27.63 | 27.19 | 28.93 | 27.84 | 26.50 | 27.18 | 28.98 | 26.43 | 26.03 | 27.01 | 43.88 | 36.10 |
| La | 34.09 | 33.83 | 30.10 | 31.19 | 32.41 | 32.91 | 44.17 | 36.95 | 38.22 | 43.43 | 54.62 | 49.92 |
| Ce | 75.52 | 75.02 | 68.90 | 71.33 | 72.55 | 72.89 | 93.02 | 80.91 | 82.54 | 93.07 | 119.90 | 109.83 |
| Pr | 9.97 | 9.50 | 9.39 | 9.51 | 9.56 | 9.69 | 10.92 | 10.07 | 10.20 | 11.56 | 14.78 | 12.36 |
| Nd | 47.38 | 48.12 | 46.47 | 46.41 | 45.61 | 46.99 | 55.88 | 47.35 | 47.19 | 53.38 | 66.40 | 58.93 |
| Sm | 11.51 | 11.46 | 11.63 | 11.25 | 11.13 | 11.25 | 12.39 | 11.05 | 11.07 | 11.84 | 15.27 | 12.42 |
| Eu | 2.54 | 2.39 | 2.76 | 2.58 | 2.41 | 2.51 | 3.17 | 2.90 | 2.97 | 3.22 | 2.93 | 2.78 |
| Gd | 7.49 | 7.54 | 7.80 | 7.65 | 7.48 | 7.68 | 7.91 | 7.21 | 7.41 | 7.88 | 10.35 | 8.31 |
| Tb | 1.18 | 1.20 | 1.25 | 1.20 | 1.15 | 1.21 | 1.25 | 1.15 | 1.14 | 1.21 | 1.68 | 1.41 |
| Dy | 6.10 | 6.05 | 6.47 | 6.21 | 5.91 | 6.05 | 6.47 | 5.93 | 5.95 | 6.31 | 9.14 | 7.19 |
| Ho | 1.13 | 1.07 | 1.20 | 1.19 | 1.11 | 1.11 | 1.20 | 1.15 | 1.11 | 1.16 | 1.71 | 1.34 |
| Er | 3.05 | 2.86 | 3.18 | 2.98 | 2.95 | 3.07 | 3.59 | 3.15 | 3.05 | 3.17 | 4.92 | 4.09 |
| Tm | 0.46 | 0.42 | 0.46 | 0.46 | 0.42 | 0.46 | 0.52 | 0.48 | 0.47 | 0.50 | 0.76 | 0.66 |
| Yb | 2.28 | 2.25 | 2.41 | 2.26 | 2.15 | 2.25 | 2.93 | 2.63 | 2.59 | 2.58 | 3.91 | 3.36 |

Table 1. Cont.

| Lithology | Epidote-Biotite-Albite Schist | | | | | | Biotite-Albite Schist | | | | | |
|----------------------------------|-------------------------------|-----------|-----------|-----------|-----------|-----------|-----------------------|-----------|-----------|-----------|-----------|-----------|
| | Sample No. | G1631-1.1 | G1631-1.2 | G1631-1.3 | G1631-1.4 | G1631-1.5 | G1631-1.6 | G1631-4.1 | G1631-4.2 | G1631-4.3 | G1631-4.4 | G1631-4.5 |
| Lu | 0.31 | 0.31 | 0.34 | 0.33 | 0.31 | 0.30 | 0.38 | 0.37 | 0.36 | 0.37 | 0.55 | 0.47 |
| ΣREE | 202.99 | 202.01 | 192.34 | 194.53 | 195.14 | 198.36 | 243.82 | 211.29 | 214.24 | 239.68 | 306.92 | 273.07 |
| LREE | 181.00 | 180.32 | 169.25 | 172.27 | 173.66 | 176.24 | 219.56 | 189.22 | 192.18 | 216.50 | 273.90 | 246.24 |
| HREE | 21.98 | 21.69 | 23.10 | 22.27 | 21.48 | 22.12 | 24.25 | 22.07 | 22.06 | 23.18 | 33.02 | 26.83 |
| L/H | 8.23 | 8.31 | 7.33 | 7.74 | 8.09 | 7.97 | 9.05 | 8.57 | 8.71 | 9.34 | 8.29 | 9.18 |
| La _N /Yb _N | 10.73 | 10.78 | 8.97 | 9.89 | 10.80 | 10.49 | 10.82 | 10.09 | 10.58 | 12.06 | 10.02 | 10.65 |
| δCe | 0.99 | 1.01 | 1.00 | 1.01 | 1.00 | 0.99 | 1.01 | 1.01 | 1.00 | 1.00 | 1.01 | 1.05 |
| δEu | 0.78 | 0.74 | 0.83 | 0.80 | 0.76 | 0.78 | 0.92 | 0.93 | 0.94 | 0.96 | 0.67 | 0.79 |
| Li | 18.58 | 20.34 | 27.07 | 22.73 | 20.42 | 21.77 | 25.75 | 25.34 | 26.55 | 29.34 | 36.92 | 40.63 |
| Sc | 14.27 | 14.17 | 15.34 | 15.52 | 15.04 | 15.69 | 11.35 | 12.81 | 12.47 | 12.44 | 13.23 | 12.99 |
| V | 401.29 | 379.56 | 347.99 | 361.07 | 417.77 | 400.93 | 107.69 | 126.32 | 111.54 | 131.04 | 202.25 | 166.49 |
| Cr | 39.74 | 43.51 | 29.62 | 42.25 | 41.89 | 39.04 | 86.51 | 82.63 | 75.99 | 82.93 | 23.71 | 36.53 |
| Co | 24.30 | 24.63 | 30.59 | 27.44 | 25.92 | 27.25 | 12.06 | 12.83 | 13.02 | 13.17 | 16.46 | 15.25 |
| Ni | 21.15 | 22.40 | 21.70 | 21.98 | 22.28 | 23.29 | 34.82 | 39.55 | 36.45 | 40.00 | 23.84 | 24.71 |
| Ga | 23.20 | 23.44 | 21.69 | 22.00 | 24.98 | 23.42 | 18.47 | 19.86 | 18.39 | 19.02 | 20.92 | 20.71 |
| Rb | 8.83 | 8.46 | 31.45 | 13.85 | 5.57 | 3.97 | 26.70 | 30.04 | 48.56 | 30.16 | 45.00 | 59.66 |
| Sr | 1100 | 1200 | 893 | 995 | 1400 | 1300 | 566 | 586 | 554 | 5408 | 944 | 942 |
| Zr | 87.75 | 61.90 | 71.92 | 73.22 | 88.55 | 80.19 | 185.02 | 176.05 | 166.34 | 168.27 | 27.95 | 51.58 |
| Nb | 10.84 | 10.27 | 11.11 | 10.74 | 9.10 | 8.95 | 15.52 | 14.40 | 14.34 | 15.77 | 30.61 | 23.04 |
| Ba | 78.40 | 106.57 | 146.80 | 113.68 | 82.57 | 71.06 | 308.28 | 357.57 | 419.52 | 400.07 | 474.22 | 591.36 |
| Hf | 0.84 | 0.75 | 0.80 | 0.81 | 0.76 | 0.83 | 0.78 | 0.66 | 0.80 | 0.74 | 0.83 | 0.64 |
| Ta | 0.85 | 0.80 | 0.85 | 0.76 | 0.87 | 0.77 | 0.67 | 0.64 | 0.68 | 0.63 | 1.60 | 1.07 |
| Th | 17.66 | 7.07 | 6.77 | 5.97 | 5.97 | 5.51 | 7.27 | 6.82 | 7.21 | 7.56 | 7.74 | 6.39 |
| U | 2.11 | 2.20 | 2.24 | 2.13 | 2.14 | 2.08 | 2.44 | 2.33 | 2.16 | 2.40 | 3.19 | 2.29 |

4.1.1. The Epidote-Biotite-Albite Schists

The epidote-biotite-albite schists had 49.28–51.15 wt% SiO₂, 3.19–3.99 wt% MgO, 15.84–16.99 wt% Al₂O₃, 1.66–1.80 wt% TiO₂, 0.03–1.28 wt% Na₂O, 0.02–0.73 wt% K₂O, 9.51–12.68 wt% CaO and 9.79–10.57 wt% total FeO. They had Mg# of [Mg# = 100 × MgO_{molar}/(MgO_{molar} + FeO_{molar})] 35.14–42.25. The Na₂O/K₂O ratios ranged from 1.56–2.98, indicating that the samples belonged to the sodium series. As can be seen from the plot of SiO₂ vs. K₂O + Na₂O and Nb/Y vs. Zr/TiO₂*0.0001 diagrams (Figure 4a–b), all of these metavolcanic rocks plot in the basalt and basaltic andesite field. On a plot of SiO₂ vs. ^TFeO/MgO (Figure 4c), the samples plot in the tholeiitic field.

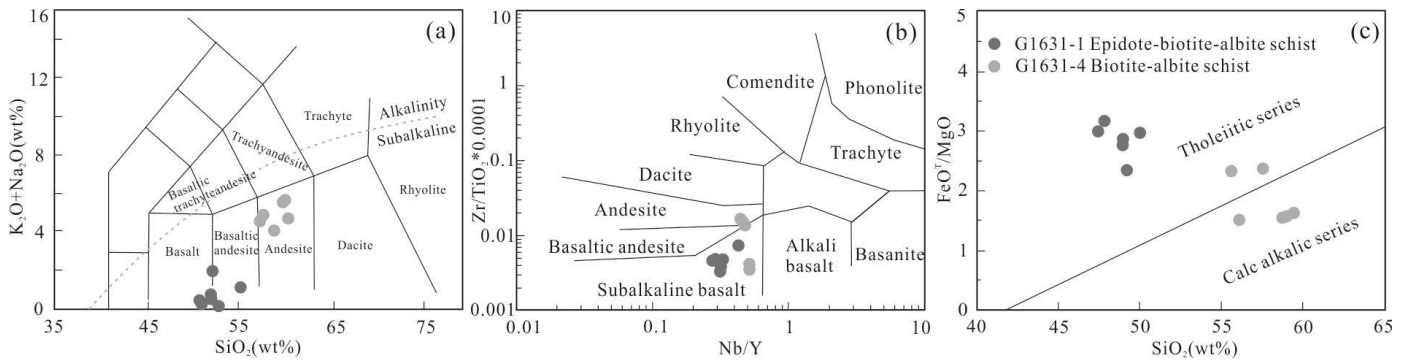


Figure 4. Classification and series diagrams of the Hadayang schists. (a) Plot of SiO₂ vs. K₂O + Na₂O (after [67]), with the alkalic/subalkalic boundary of [68] shown; (b) plot of Zr/TiO₂*0.0001 vs. Nb/Y (after [69]); (c) plot of ^TFeO/MgO vs. SiO₂ (after [70]).

The epidote-biotite-albite schists had total rare earth element (REE) concentrations from 194.53 to 202.99 ppm, with an average value of 197.56 ppm. On the chondrite-normalized REE diagram (Figure 5a), the light rare earth elements (LREEs) are moderately enriched relative to the heavy rare earth elements (HREEs) with (La/Yb)_N ratios ranging from 8.97 to 10.78, while the HREEs are relatively flat. These metavolcanic rocks had slightly negative Eu anomalies ($\delta\text{Eu} = 0.74\text{--}0.83$). The primitive-mantle-normalized incompatible element diagrams (Figure 5b) show that the epidote-biotite-albite schists were relatively enriched in large ion lithophile elements (LILEs) (such as Rb, Ba, Th and U) relative to high-field-strength elements (HFSEs) (such as Nb, P and Ti).

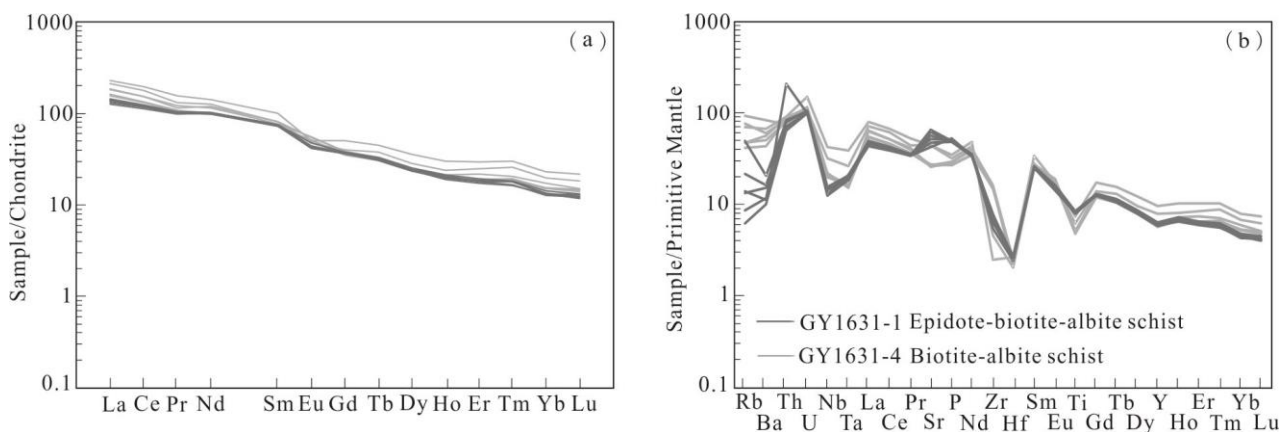


Figure 5. Chondrite-normalized REE patterns (a) and primitive-mantle-normalized trace element spidergrams (b) for the Hadayang schists. Normalization values are taken from [71,72].

4.1.2. The Biotite-Albite Schists

The biotite-albite schists had SiO₂ of 57.59–60.69 wt% and high TiO₂ (1.05–1.62 wt%), ΣFeO (6.63–7.81 wt%) and Al₂O₃ (16.47–17.21 wt%). Their alkalis (K₂O + Na₂O) ranged

from 4.26 to 5.77 wt%, and the low K_2O/Na_2O ratio (0.16 to 0.74) indicated that the samples belonged to the sodium series. All of the samples plot in the andesite field on a SiO_2 vs. $Na_2O + K_2O$ diagram (Figure 4a). As can be seen from the plot of $Zr/TiO_2 \times 0.0001$ vs. Nb/Y (Figure 4b), most of the samples plot in the subalkaline basalt and andesite fields. On the other hand, on the plot of FeO^T/MgO vs. SiO_2 , except for two samples that fall into the tholeiitic field, the biotite-albite schist samples plot in the calc-alkaline field.

The biotite-albite schists had variable total rare earth element (REE) concentrations from 211.29 to 306.92 ppm, with an average value of 248.17 ppm. These metavolcanic rocks exhibited LREEs enrichment ($(La/Yb)_N = 10.02\text{--}12.06$) and slight negative Eu anomalies ($\delta Eu = 0.67\text{--}0.96$) (Figure 5a). On a primitive-mantle-normalized trace element plot (Figure 5b), the biotite-albite schist samples also appear as enriched in large ion lithophile elements (LILEs) relative to the high-field-strength elements (HFSEs), which were similar to those in the epidote-biotite-albite schists.

4.2. Zircon U-Pb Dating

Cathodoluminescence (CL) images and concordia plots for the analyzed zircons are shown in Figure 6. Zircons from the epidote-biotite-albite schist sample (G1631-1) and biotite-albite schist sample (G1631-4) were mainly euhedral and elongate, with aspect ratios of 1:1–2:1. They showed straight rhythmic stripes, typical oscillatory zoning or sector zoning in CL images (Figure 6), with high Th/U ratios (0.49–1.38, Table 2), which is characteristic of magmatic zircons [73]. In total, 60 concordant $^{206}Pb/^{238}U$ ages, obtained from 70 zircon grains, ranged from 338 to 370 Ma. Two samples yielded similar zircon U-Pb ages around 360 Ma (Figure 7), with weighted mean $^{206}Pb/^{238}U$ ages of 360 ± 2 Ma (G1631-1, $n = 35$, MSWD = 1.4) and 355 ± 3 Ma (G1631-4, $n = 35$, MSWD = 2.1). The two ages were interpreted as the crystallization ages of the magmatic protolith of the two schists.

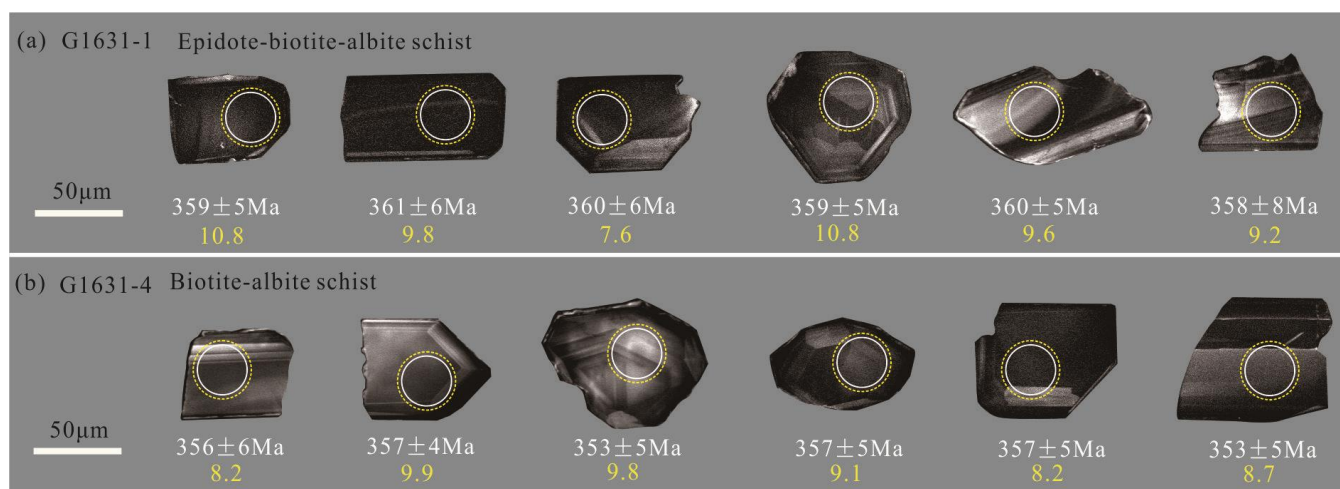


Figure 6. Cathodoluminescence images of zircon grains selected for analysis from the epidote-biotite-albite schist (a) and biotite-albite schist (b). The smaller white circles represent locations of LA-ICP-MS U-Pb dating, whereas the bigger yellow circles (dotted line) indicate locations of Hf isotopic analyses.

Table 2. LA-ICP-MS zircon U-Pb dating results for the Hadayang schists.

| Analytical No. | Th (10 ⁻⁶) | U (10 ⁻⁶) | Th/U | Isotopic Ratio | | | | | | Age (Ma) | | | | | | Concordance |
|---------------------------------------|---------------------------|--------------------------|------|-------------------------------------|--------|-------------------------------------|--------|--------------------------------------|--------|-------------------------------------|----|-------------------------------------|----|--------------------------------------|----|-------------|
| | | | | ²⁰⁶ Pb/ ²³⁸ U | | ²⁰⁷ Pb/ ²³⁵ U | | ²⁰⁷ Pb/ ²⁰⁶ Pb | | ²⁰⁶ Pb/ ²³⁸ U | | ²⁰⁷ Pb/ ²³⁵ U | | ²⁰⁷ Pb/ ²⁰⁶ Pb | | |
| | | | | Ratio | 1σ | Ratio | 1σ | Ratio | 1σ | Age | 1σ | Age | 1σ | Age | 1σ | |
| G1631-1 Epidote biotite albite schist | | | | | | | | | | | | | | | | |
| 1 | 334.7 | 354.2 | 0.94 | 0.0582 | 0.0011 | 0.4358 | 0.0097 | 0.0543 | 0.0008 | 365 | 7 | 367 | 7 | 387 | 32 | 99.5% |
| 2 | 551.7 | 501.4 | 1.10 | 0.0601 | 0.0009 | 0.4499 | 0.0080 | 0.0543 | 0.0006 | 376 | 5 | 377 | 6 | 389 | 19 | 99.7% |
| 3 | 484.3 | 436.0 | 1.11 | 0.0573 | 0.0008 | 0.4235 | 0.0067 | 0.0537 | 0.0007 | 359 | 5 | 359 | 5 | 367 | 28 | 100.0% |
| 4 | 1201.1 | 1055.1 | 1.14 | 0.0589 | 0.0010 | 0.4434 | 0.0073 | 0.0547 | 0.0005 | 369 | 6 | 373 | 5 | 398 | 16 | 98.9% |
| 5 | 640.3 | 554.4 | 1.15 | 0.0576 | 0.0011 | 0.4249 | 0.0077 | 0.0536 | 0.0007 | 361 | 7 | 360 | 6 | 354 | 30 | 99.7% |
| 6 | 1369.8 | 927.8 | 1.48 | 0.0582 | 0.0010 | 0.4373 | 0.0075 | 0.0545 | 0.0006 | 365 | 6 | 368 | 5 | 391 | 24 | 99.2% |
| 7 | 610.1 | 586.2 | 1.04 | 0.0591 | 0.0009 | 0.4304 | 0.0073 | 0.0529 | 0.0007 | 370 | 5 | 364 | 5 | 324 | 30 | 98.4% |
| 8 | 550.6 | 744.5 | 0.74 | 0.0585 | 0.0009 | 0.4291 | 0.0062 | 0.0533 | 0.0006 | 366 | 5 | 363 | 4 | 339 | 24 | 99.2% |
| 9 | 691.4 | 608.9 | 1.14 | 0.0578 | 0.0008 | 0.4215 | 0.0066 | 0.0528 | 0.0006 | 362 | 5 | 357 | 5 | 320 | 24 | 98.6% |
| 10 | 1105.5 | 1001.7 | 1.10 | 0.0575 | 0.0008 | 0.4288 | 0.0065 | 0.0541 | 0.0005 | 360 | 5 | 362 | 5 | 372 | 20 | 99.4% |
| 11 | 475.6 | 522.9 | 0.91 | 0.0570 | 0.0009 | 0.4269 | 0.0072 | 0.0543 | 0.0006 | 357 | 5 | 361 | 5 | 383 | 21 | 98.9% |
| 12 | 1172.7 | 909.3 | 1.29 | 0.0583 | 0.0008 | 0.4349 | 0.0063 | 0.0541 | 0.0005 | 365 | 5 | 367 | 5 | 376 | 20 | 99.5% |
| 13 | 168.8 | 288.6 | 0.59 | 0.0565 | 0.0008 | 0.4316 | 0.0069 | 0.0554 | 0.0007 | 354 | 5 | 364 | 5 | 432 | 5 | 97.2% |
| 14 | 230.1 | 272.5 | 0.84 | 0.0563 | 0.0009 | 0.4239 | 0.0084 | 0.0546 | 0.0008 | 353 | 5 | 359 | 6 | 395 | 36 | 98.3% |
| 15 | 473.3 | 483.8 | 0.98 | 0.0568 | 0.0008 | 0.4233 | 0.0070 | 0.0540 | 0.0006 | 356 | 5 | 358 | 5 | 372 | 24 | 99.4% |
| 16 | 1575.6 | 1139.1 | 1.38 | 0.0574 | 0.0009 | 0.4213 | 0.0071 | 0.0532 | 0.0005 | 360 | 6 | 357 | 5 | 345 | 22 | 99.2% |
| 17 | 480.5 | 534.4 | 0.90 | 0.0569 | 0.0014 | 0.4268 | 0.0189 | 0.0539 | 0.0013 | 357 | 8 | 361 | 14 | 365 | 49 | 98.9% |
| 18 | 656.6 | 584.9 | 1.12 | 0.0571 | 0.0008 | 0.4252 | 0.0068 | 0.0544 | 0.0007 | 358 | 5 | 360 | 5 | 387 | 25 | 99.4% |
| 19 | 1081.4 | 877.1 | 1.23 | 0.0574 | 0.0008 | 0.4238 | 0.0076 | 0.0535 | 0.0006 | 360 | 5 | 359 | 5 | 350 | 32 | 99.7% |
| 20 | 740.6 | 669.2 | 1.11 | 0.0558 | 0.0009 | 0.4160 | 0.0083 | 0.0539 | 0.0006 | 350 | 5 | 353 | 6 | 365 | 24 | 99.1% |
| 21 | 538.6 | 513.2 | 1.05 | 0.0579 | 0.0010 | 0.4330 | 0.0073 | 0.0543 | 0.0007 | 363 | 6 | 365 | 5 | 383 | 21 | 99.5% |
| 22 | 254.0 | 298.4 | 0.85 | 0.0567 | 0.0009 | 0.4244 | 0.0073 | 0.0544 | 0.0008 | 355 | 6 | 359 | 5 | 387 | 33 | 98.9% |
| 23 | 1794.4 | 1046.2 | 1.72 | 0.0590 | 0.0010 | 0.4334 | 0.0067 | 0.0533 | 0.0005 | 369 | 6 | 366 | 5 | 343 | 22 | 99.2% |
| 24 | 683.2 | 584.2 | 1.17 | 0.0572 | 0.0008 | 0.4321 | 0.0075 | 0.0547 | 0.0006 | 359 | 5 | 365 | 5 | 398 | 22 | 98.3% |
| 25 | 292.0 | 374.7 | 0.78 | 0.0574 | 0.0008 | 0.4210 | 0.0072 | 0.0532 | 0.0007 | 360 | 5 | 357 | 5 | 345 | 28 | 99.2% |
| 26 | 410.1 | 476.3 | 0.86 | 0.0572 | 0.0009 | 0.4236 | 0.0074 | 0.0538 | 0.0007 | 358 | 6 | 359 | 5 | 365 | 23 | 99.7% |
| 27 | 188.0 | 248.3 | 0.76 | 0.0579 | 0.0011 | 0.4308 | 0.0082 | 0.0541 | 0.0007 | 363 | 6 | 364 | 7 | 376 | 30 | 99.7% |
| 28 | 1332.8 | 971.5 | 1.37 | 0.0556 | 0.0007 | 0.4076 | 0.0059 | 0.0532 | 0.0006 | 349 | 5 | 347 | 4 | 345 | 19 | 99.4% |
| 29 | 334.7 | 354.2 | 0.94 | 0.0582 | 0.0011 | 0.4358 | 0.0097 | 0.0543 | 0.0008 | 365 | 7 | 367 | 7 | 387 | 32 | 99.5% |
| 30 | 551.7 | 501.4 | 1.10 | 0.0601 | 0.0009 | 0.4499 | 0.0080 | 0.0543 | 0.0006 | 376 | 5 | 377 | 6 | 389 | 19 | 99.7% |
| 31 | 484.3 | 436.0 | 1.11 | 0.0573 | 0.0008 | 0.4235 | 0.0067 | 0.0537 | 0.0007 | 359 | 5 | 359 | 5 | 367 | 28 | 100.0% |
| 32 | 1201.1 | 1055.1 | 1.14 | 0.0589 | 0.0010 | 0.4434 | 0.0073 | 0.0547 | 0.0005 | 369 | 6 | 373 | 5 | 398 | 16 | 98.9% |
| 33 | 640.3 | 554.4 | 1.15 | 0.0576 | 0.0011 | 0.4249 | 0.0077 | 0.0536 | 0.0007 | 361 | 7 | 360 | 6 | 354 | 30 | 99.7% |
| 34 | 1369.8 | 927.8 | 1.48 | 0.0582 | 0.0010 | 0.4373 | 0.0075 | 0.0545 | 0.0006 | 365 | 6 | 368 | 5 | 391 | 24 | 99.2% |
| 35 | 610.1 | 586.2 | 1.04 | 0.0591 | 0.0009 | 0.4304 | 0.0073 | 0.0529 | 0.0007 | 370 | 5 | 364 | 5 | 324 | 30 | 98.4% |

Table 2. Cont.

| Analytical No. | Th (10 ⁻⁶) | U (10 ⁻⁶) | Th/U | Isotopic Ratio | | | | | | Age (Ma) | | | | Concordance | | |
|--|---------------------------|--------------------------|------|-------------------------------------|--------|-------------------------------------|--------|--------------------------------------|--------|-------------------------------------|----|-------------------------------------|-----|-------------|--------------------------------------|--------|
| | | | | ²⁰⁶ Pb/ ²³⁸ U | | ²⁰⁷ Pb/ ²³⁵ U | | ²⁰⁷ Pb/ ²⁰⁶ Pb | | ²⁰⁶ Pb/ ²³⁸ U | | ²⁰⁷ Pb/ ²³⁵ U | | | ²⁰⁷ Pb/ ²⁰⁶ Pb | |
| | | | | Ratio | 1σ | Ratio | 1σ | Ratio | 1σ | Age | 1σ | Age | 1σ | | Age | 1σ |
| G1631-4 Chlorite epidote biotite albite schist | | | | | | | | | | | | | | | | |
| 1 | 414.8 | 339.8 | 1.22 | 0.0568 | 0.0010 | 0.4355 | 0.0077 | 0.0557 | 0.0008 | 356 | 6 | 367 | 5 | 443 | 32 | 97.0% |
| 2 | 268.7 | 273.3 | 0.98 | 0.0571 | 0.0007 | 0.4433 | 0.0102 | 0.0561 | 0.0010 | 358 | 5 | 373 | 7 | 458 | 41 | 95.9% |
| 3 | 211.8 | 198.9 | 1.06 | 0.0571 | 0.0008 | 0.4344 | 0.0087 | 0.0552 | 0.0009 | 358 | 5 | 366 | 6 | 420 | 35 | 97.8% |
| 4 | 285.3 | 300.2 | 0.95 | 0.0570 | 0.0007 | 0.4223 | 0.0078 | 0.0537 | 0.0008 | 357 | 4 | 358 | 6 | 367 | 33 | 99.7% |
| 5 | 161.0 | 296.5 | 0.54 | 0.0581 | 0.0009 | 0.4377 | 0.0092 | 0.0546 | 0.0008 | 364 | 6 | 369 | 7 | 395 | 33 | 98.6% |
| 6 | 52.5 | 100.1 | 0.52 | 0.0577 | 0.0009 | 0.4436 | 0.0124 | 0.0558 | 0.0014 | 362 | 6 | 373 | 9 | 456 | 54 | 97.0% |
| 7 | 91.9 | 110.7 | 0.83 | 0.0562 | 0.0009 | 0.4195 | 0.0109 | 0.0541 | 0.0012 | 353 | 5 | 356 | 8 | 376 | 53 | 99.2% |
| 8 | 321.8 | 326.1 | 0.99 | 0.0570 | 0.0011 | 0.4262 | 0.0100 | 0.0542 | 0.0008 | 358 | 7 | 361 | 7 | 389 | 33 | 99.2% |
| 9 | 133.0 | 179.9 | 0.74 | 0.0555 | 0.0008 | 0.4124 | 0.0084 | 0.0540 | 0.0010 | 348 | 5 | 351 | 6 | 372 | 39 | 99.1% |
| 10 | 138.7 | 284.9 | 0.49 | 0.0561 | 0.0010 | 0.4062 | 0.0084 | 0.0526 | 0.0009 | 352 | 6 | 346 | 6 | 322 | 37 | 98.3% |
| 11 | 209.1 | 210.6 | 0.99 | 0.0551 | 0.0008 | 0.4075 | 0.0072 | 0.0537 | 0.0008 | 346 | 5 | 347 | 5 | 367 | 35 | 99.7% |
| 12 | 459.3 | 411.0 | 1.12 | 0.0580 | 0.0016 | 0.4238 | 0.0116 | 0.0531 | 0.0008 | 363 | 10 | 359 | 8 | 345 | 32 | 98.9% |
| 13 | 189.4 | 209.4 | 0.90 | 0.0582 | 0.0010 | 0.4482 | 0.0129 | 0.0557 | 0.0013 | 365 | 6 | 376 | 9 | 439 | 50 | 97.0% |
| 14 | 348.6 | 343.1 | 1.02 | 0.0587 | 0.0011 | 0.4316 | 0.0087 | 0.0534 | 0.0008 | 368 | 7 | 364 | 6 | 346 | 27 | 98.9% |
| 15 | 159.3 | 192.3 | 0.83 | 0.0573 | 0.0010 | 0.4323 | 0.0103 | 0.0547 | 0.0010 | 359 | 6 | 365 | 7 | 398 | 36 | 98.3% |
| 16 | 102.2 | 129.5 | 0.79 | 0.0581 | 0.0014 | 0.4235 | 0.0146 | 0.0532 | 0.0016 | 364 | 8 | 359 | 10 | 345 | 67 | 98.6% |
| 17 | 151.1 | 170.2 | 0.89 | 0.0570 | 0.0009 | 0.4050 | 0.0103 | 0.0515 | 0.0011 | 357 | 5 | 345 | 8 | 261 | 50 | 96.6% |
| 18 | 128.2 | 179.6 | 0.71 | 0.0572 | 0.0009 | 0.4192 | 0.0087 | 0.0532 | 0.0010 | 359 | 5 | 356 | 6 | 339 | 47 | 99.2% |
| 19 | 212.1 | 226.9 | 0.93 | 0.0543 | 0.0009 | 0.4159 | 0.0104 | 0.0553 | 0.0010 | 341 | 6 | 353 | 7.5 | 433 | 39 | 96.5% |
| 20 | 163.6 | 203.1 | 0.81 | 0.0555 | 0.0009 | 0.4156 | 0.0084 | 0.0544 | 0.0009 | 348 | 6 | 353 | 6 | 391 | 39 | 98.6% |
| 21 | 380.3 | 405.1 | 0.94 | 0.0553 | 0.0009 | 0.4168 | 0.0085 | 0.0546 | 0.0007 | 347 | 6 | 354 | 6 | 395 | 34 | 98.0% |
| 22 | 145.1 | 179.4 | 0.81 | 0.0538 | 0.0007 | 0.4009 | 0.0087 | 0.0539 | 0.0010 | 338 | 4 | 342 | 6 | 367 | 43 | 98.8% |
| 23 | 420.8 | 585.3 | 0.72 | 0.0546 | 0.0008 | 0.3950 | 0.0067 | 0.0523 | 0.0006 | 343 | 5 | 338 | 5 | 302 | 24 | 98.5% |
| 24 | 110.9 | 133.7 | 0.83 | 0.0570 | 0.0008 | 0.4283 | 0.0118 | 0.0546 | 0.0015 | 357 | 5 | 362 | 8 | 395 | 61 | 98.6% |
| 25 | 70.2 | 127.1 | 0.55 | 0.0575 | 0.0007 | 0.4186 | 0.0105 | 0.0526 | 0.0011 | 360 | 5 | 355 | 8 | 322 | 51 | 98.6% |
| 26 | 141.9 | 153.0 | 0.93 | 0.0579 | 0.0009 | 0.4224 | 0.0100 | 0.0529 | 0.0011 | 363 | 5 | 358 | 7 | 324 | 48 | 98.6% |
| 27 | 122.8 | 179.0 | 0.69 | 0.0572 | 0.0008 | 0.4239 | 0.0085 | 0.0537 | 0.0010 | 359 | 5 | 359 | 6 | 361 | 39 | 100.0% |
| 28 | 245.0 | 234.4 | 1.05 | 0.0584 | 0.0012 | 0.4403 | 0.0145 | 0.0547 | 0.0015 | 366 | 7 | 371 | 10 | 467 | 58 | 98.6% |
| 29 | 249.3 | 250.8 | 0.99 | 0.0569 | 0.0010 | 0.4200 | 0.0093 | 0.0536 | 0.0010 | 357 | 6 | 356 | 7 | 354 | 47 | 99.7% |
| 30 | 369.7 | 389.9 | 0.95 | 0.0563 | 0.0009 | 0.4113 | 0.0065 | 0.0530 | 0.0006 | 353 | 6 | 350 | 5 | 328 | 32 | 99.1% |
| 31 | 337.6 | 274.2 | 1.23 | 0.0552 | 0.0008 | 0.3943 | 0.0079 | 0.0516 | 0.0007 | 346 | 5 | 338 | 6 | 265 | 32 | 97.7% |
| 32 | 414.8 | 339.8 | 1.22 | 0.0568 | 0.0010 | 0.4355 | 0.0077 | 0.0557 | 0.0008 | 356 | 6 | 367 | 5 | 443 | 32 | 97.0% |
| 33 | 268.7 | 273.3 | 0.98 | 0.0571 | 0.0007 | 0.4433 | 0.0102 | 0.0561 | 0.0010 | 358 | 5 | 373 | 7 | 458 | 41 | 95.9% |
| 34 | 211.8 | 198.9 | 1.06 | 0.0571 | 0.0008 | 0.4344 | 0.0087 | 0.0552 | 0.0009 | 358 | 5 | 366 | 6 | 420 | 35 | 97.8% |
| 35 | 285.3 | 300.2 | 0.95 | 0.0570 | 0.0007 | 0.4223 | 0.0078 | 0.0537 | 0.0008 | 357 | 4 | 358 | 7 | 367 | 33 | 99.7% |

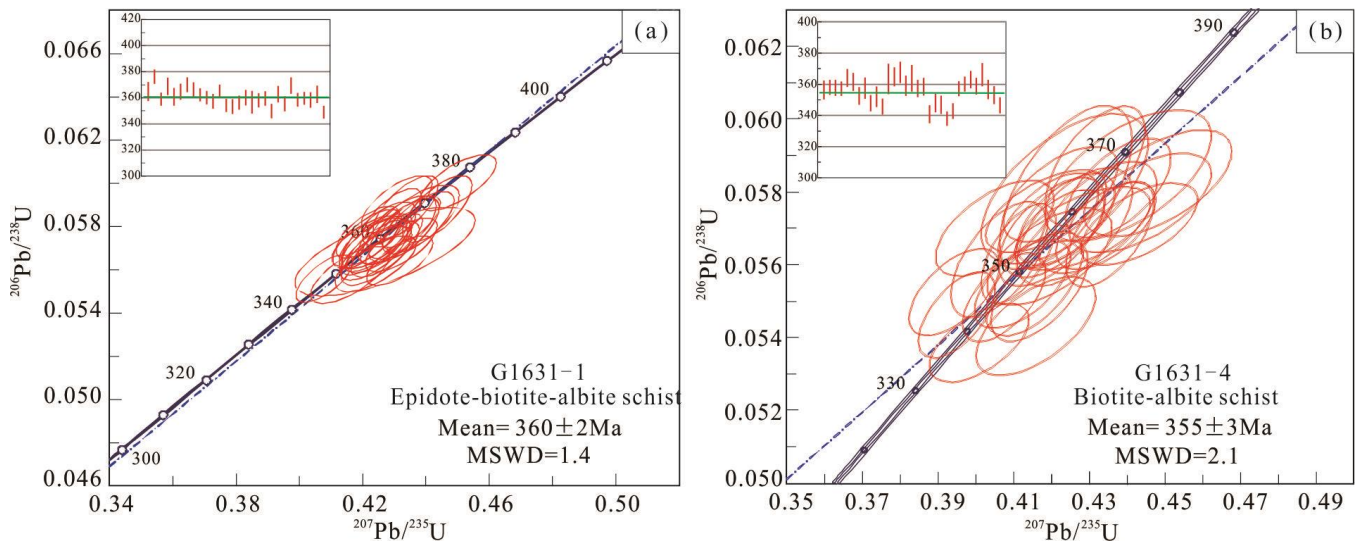


Figure 7. U-Pb concordia and weighted mean ages for the epidote-biotite-albite schist (a) and biotite-albite schist (b).

4.3. Zircon Hf Isotopies

The zircons from the epidote-biotite-albite schist (sample G1631-1) had homogeneous $^{176}\text{Hf}/^{177}\text{Hf}$ ratios of 0.282749 to 0.282872, with $\epsilon\text{Hf}(t)$ values of +6.5 to +11.0 (Figure 8), one-stage Hf model (T_{DM1}) ages from 552 to 746 Ma and two-stage Hf model (T_{DM2}) ages from 661 to 902 Ma. Similarly, the zircons from the biotite-albite schist sample (sample G1631-4) also possessed relatively homogeneous Hf isotopic compositions of 0.282783 to 0.282870, $\epsilon\text{Hf}(t)$ values of +7.9 to +10.9 (Figure 8), T_{DM1} ages from 547 to 649 Ma and T_{DM2} ages from 660 to 859 Ma (Table 3). All of these characteristics indicate that the parent magmas of the Hadayang schists were produced from a relatively depleted mantle source.

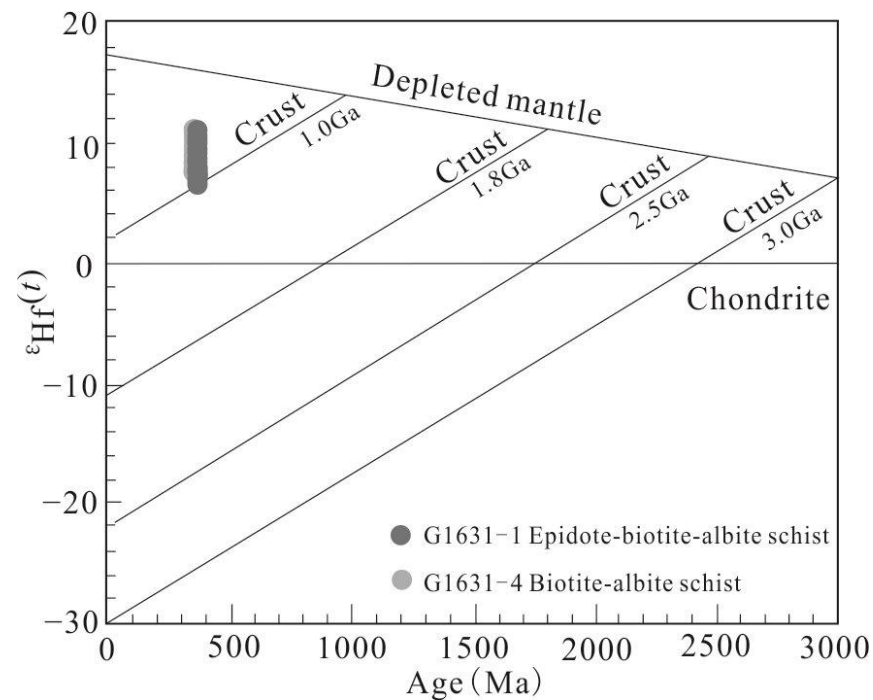


Figure 8. Diagrams of zircon Hf isotopic of the Hadayang schists.

Table 3. In situ zircon Lu-Hf isotopic results for the Hadayang schists.

| Analytical Spot | t (Ma) | $^{176}\text{Yb}/^{177}\text{Hf}$ | $^{176}\text{Lu}/^{177}\text{Hf}$ | $^{176}\text{Hf}/^{177}\text{Hf}$ | I_{Hf} | $\epsilon_{\text{Hf}}(0)$ | $\epsilon_{\text{Hf}}(t)$ | $T_{\text{DM1}}(\text{Hf})$ (Ma) | $T_{\text{DM2}}(\text{Hf})$ (Ma) | $f_{\text{Lu/Hf}}$ |
|---------------------------------------|--------|-----------------------------------|-----------------------------------|-----------------------------------|-----------------|---------------------------|---------------------------|----------------------------------|----------------------------------|--------------------|
| G1631-1 Epidote-biotite-albite schist | | | | | | | | | | |
| 1 | 365 | 0.065324 | 0.001772 | 0.282827 | 0.282815 | 2.0 | 9.6 | 615 | 756 | −0.95 |
| 2 | 359 | 0.069656 | 0.001920 | 0.282866 | 0.282853 | 3.3 | 10.8 | 560 | 672 | −0.94 |
| 3 | 361 | 0.082890 | 0.002175 | 0.282798 | 0.282783 | 0.9 | 8.3 | 665 | 832 | −0.93 |
| 4 | 362 | 0.053714 | 0.001471 | 0.282834 | 0.282824 | 2.2 | 9.8 | 600 | 737 | −0.96 |
| 5 | 360 | 0.112169 | 0.002980 | 0.282772 | 0.282752 | 0.0 | 7.2 | 718 | 902 | −0.91 |
| 6 | 357 | 0.056043 | 0.001614 | 0.282853 | 0.282842 | 2.9 | 10.3 | 576 | 701 | −0.95 |
| 7 | 360 | 0.059902 | 0.001785 | 0.282776 | 0.282764 | 0.1 | 7.6 | 690 | 876 | −0.95 |
| 8 | 357 | 0.092929 | 0.002522 | 0.282821 | 0.282804 | 1.7 | 9.0 | 637 | 787 | −0.92 |
| 9 | 358 | 0.056231 | 0.001558 | 0.282795 | 0.282785 | 0.8 | 8.3 | 657 | 829 | −0.95 |
| 10 | 360 | 0.088918 | 0.002387 | 0.282836 | 0.28282 | 2.3 | 9.6 | 612 | 748 | −0.93 |
| 11 | 363 | 0.093148 | 0.002687 | 0.282749 | 0.282731 | −0.8 | 6.5 | 746 | 948 | −0.92 |
| 12 | 359 | 0.069427 | 0.001865 | 0.282872 | 0.282859 | 3.5 | 11.0 | 552 | 661 | −0.94 |
| 13 | 360 | 0.023950 | 0.000701 | 0.282780 | 0.282775 | 0.3 | 8.0 | 664 | 850 | −0.98 |
| 14 | 358 | 0.064122 | 0.002020 | 0.282823 | 0.282809 | 1.8 | 9.2 | 625 | 773 | −0.94 |
| 15 | 363 | 0.047436 | 0.001443 | 0.282801 | 0.282791 | 1.0 | 8.7 | 647 | 812 | −0.96 |
| G1631-4 Biotite-albite schist | | | | | | | | | | |
| 1 | 356 | 0.050095 | 0.001393 | 0.282794 | 0.282785 | 0.8 | 8.3 | 655 | 829 | −0.96 |
| 2 | 358 | 0.034306 | 0.000991 | 0.282851 | 0.282844 | 2.8 | 10.4 | 569 | 695 | −0.97 |
| 3 | 358 | 0.033785 | 0.000965 | 0.282789 | 0.282782 | 0.6 | 8.2 | 656 | 835 | −0.97 |
| 4 | 357 | 0.071549 | 0.002065 | 0.282846 | 0.282832 | 2.6 | 10.0 | 593 | 723 | −0.94 |
| 5 | 364 | 0.031583 | 0.000947 | 0.282801 | 0.282794 | 1.0 | 8.8 | 639 | 804 | −0.97 |
| 6 | 353 | 0.050729 | 0.001448 | 0.282840 | 0.28283 | 2.4 | 9.8 | 592 | 731 | −0.96 |
| 7 | 358 | 0.105460 | 0.003007 | 0.282851 | 0.282831 | 2.8 | 10.0 | 600 | 724 | −0.91 |
| 8 | 352 | 0.050404 | 0.001402 | 0.282870 | 0.282861 | 3.5 | 10.9 | 547 | 660 | −0.96 |
| 9 | 359 | 0.030825 | 0.000972 | 0.282847 | 0.28284 | 2.7 | 10.3 | 574 | 703 | −0.97 |
| 10 | 357 | 0.059140 | 0.001785 | 0.282820 | 0.282808 | 1.7 | 9.1 | 625 | 776 | −0.95 |
| 11 | 359 | 0.059194 | 0.001850 | 0.282783 | 0.282771 | 0.4 | 7.9 | 679 | 859 | −0.94 |
| 12 | 357 | 0.074471 | 0.002239 | 0.282795 | 0.28278 | 0.8 | 8.2 | 669 | 839 | −0.93 |
| 13 | 359 | 0.062644 | 0.001924 | 0.282823 | 0.28281 | 1.8 | 9.2 | 624 | 772 | −0.94 |
| 14 | 357 | 0.056902 | 0.001824 | 0.282832 | 0.28282 | 2.1 | 9.6 | 609 | 751 | −0.95 |
| 15 | 353 | 0.081466 | 0.002392 | 0.282814 | 0.282798 | 1.5 | 8.7 | 645 | 802 | −0.93 |

5. Discussion

5.1. Protolith Restoration

The trace elements of the Hadayang schists were generally enriched in LILEs and depleted of HFSEs, $\text{Sr}/\text{Ba} > 1$, $\text{Cr}/\text{Ni} > 1$. Furthermore, the samples retained the crystalloblasts, which indicates that Hadayang schists should be a metaigneous rock. On a plot of A-C-FM diagram (Figure 9a), the epidote-biotite-albite schist samples plot in the calc-silicate rock and quartzite and basic volcanic rocks and ferrous-dolomitic tuff fields, while the biotite-albite schist samples plot in the intermediate-acid volcanic rock field. As can be seen from the plot of K vs. A (Figure 9b), all of the samples were igneous rock. On the other hand, on the $(\text{al} + \text{fm}) - (\text{c} + \text{alk})$ vs. Si diagram (Figure 9c), all the samples were volcanic rocks.

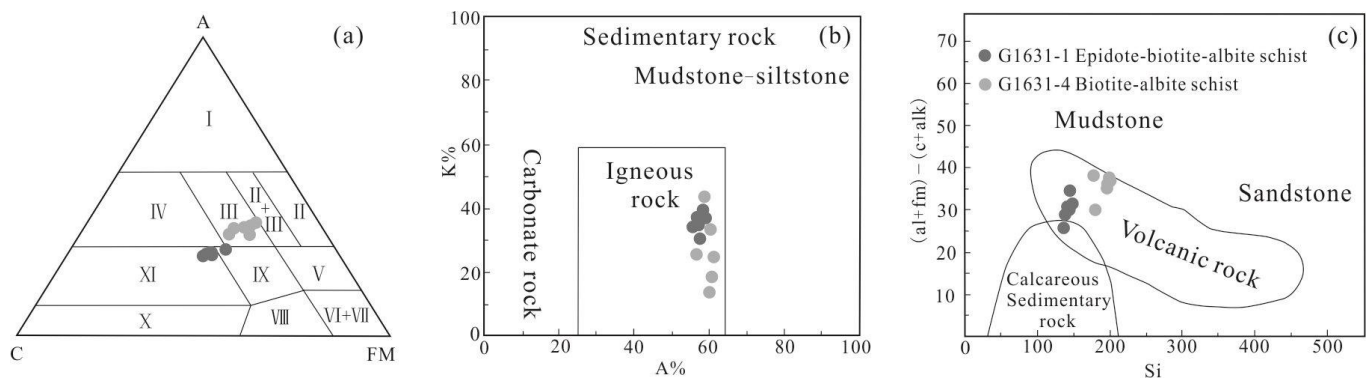


Figure 9. Classification diagrams of the Hadayang schists. (a) A-C-FM diagram (after [74]) (I—claystone and acidic volcanic rock; II—claystone and subgrauwacke; II+III—intermediate-felsic volcanic rock and subgrauwacke; III—intermediate volcanic rock; IV—arkose; V—tuffaceous siltstone; IX—basic volcanic rock and ferric dolomitic marlite; XI—calcium silicate rock and quartzite; X—calcium silicate rock; VIII—ultrabasic rock; VI+VII—silico-ferric sedimentary rock and ultrabasic rock); (b) A-K diagram (after [75]); (c) $(al + fm) - (c + alk)$ -Si diagram (after [75]).

According to the comprehensive analysis of geochemical and petrographic characteristics, the protolith of Hadayang schist was a set of intermediate-basic volcanic rocks, among which the protolith of the epidotite-biotite-albite schist was a basalt, and the protolith of the biotite-albite schist was andesite.

5.2. Geochronological Framework

The Hadayang schists were previously considered to be Precambrian in age [76], but our chronological data indicate that they formed in the Late Devonian to Early Carboniferous period. Although the magmatic activity in this period was relatively weak in the region [77], in recent years, Late Devonian–Early Carboniferous magmatic rocks have been successively identified in the XB, such as in the Yakeshi-Huolongmen, Handagai, Nenjiang and Zhalantun-Zhalaite areas. The Late Devonian–Early Carboniferous magmatic rocks in the Yakeshi-Huolongmen area include rhyolite (ca. 364–379 Ma) [78], basalt (373 ± 5 Ma) [79], diorite (381 ± 2 Ma) [77] and gabbro (ca. 341–344 Ma) [78]. Biotite granite (364 ± 4 Ma) [80] and monzonitic granite (379 ± 4 Ma) [81] are found in the Handagai area. Silicic volcanic rocks (ca. 352–354 Ma) [16,58,59], monzonitic granite (352 ± 1 Ma) [16], syenite granite (381 ± 2 Ma) [60], hornblende gabbro (363 ± 1 Ma) [61] and hornblende rock (362 ± 1 Ma) [61] have been identified in the Nenjiang area. A large number of Late Devonian–Early Carboniferous granites, including alkali feldspar granite, syenite granite, monzonitic granite and granodiorite, with ages ranging from ca. 343 to 379 Ma [13,16,77,78,80–85], were exposed in the Zhalantun-Zhalaite Banner area. In addition, there are some basic–intermediate magmatic rocks scattered in this area, including andesite (ca. 346–362 Ma) [14,86,87], basaltic andesite (373 ± 3 Ma) [88], quartz diorite (ca. 357–359 Ma) [16,78], gabbro diorite (350 ± 1 Ma) [78] and gabbro (353 ± 2 Ma) [59]. In summary, a magmatic activity occurred in the XB during the Late Devonian–Early Carboniferous period, but the tectonic significance of this magmatic event is still controversial.

5.3. Petrogenesis

5.3.1. Crustal Contamination

Before using the elemental and isotopic compositions of the samples to discuss the petrogenesis of the schists, we first assess the effects of post-magmatic alteration. The protolith of the Hadayang schists was an intermediate-basic volcanic rock, which had undergone greenschist facies metamorphism under the influence of regional metamorphism in a later period, which is supported by their LOI content of 2.23–4.05 wt% and the fact that some of the minerals had been partially replaced by chlorite and epidote. After rock metamorphism, high-field-strength elements (HFSEs), such as REEs, Y, Th, U, Zr,

Hf, Ti, Nb, Ta, etc., tend to exhibit inert migration characteristics without significant migration [89], so the characteristics of HFSEs can better reflect the protolith characteristics of metamorphic rocks.

Mantle-derived magma will inevitably be subjected to crustal contamination during the ascent process [90]. The crustal material is characterized by low Nb/La, Sm/Nd, Nb/Ta and Mg#, and high Th/La, La/Sm and SiO₂. Therefore, Mg# is positively correlated with the ratios of Nb/La, Nb/Ta and Sm/Nd, and negatively correlated with Th/La, La/Sm and SiO₂, which can indicate crustal contamination [91]. As can be seen from Figure 10, Mg# was positively correlated with Nb/La, Nb/Ta, Th/La, La/Sm and SiO₂, and negatively correlated with Sm/Nd, which is significantly different from the characteristics of crustal contamination. In addition, the Hadayang schists had significantly depleted Zr and Hf elements (Figure 5b), excluding inherited zircons, and had positive $\epsilon_{\text{Hf}}(t)$ values of +5.8 to +9.3, suggesting that crustal contamination was not a significant factor during the magmatic evolution of the Hadayang schists.

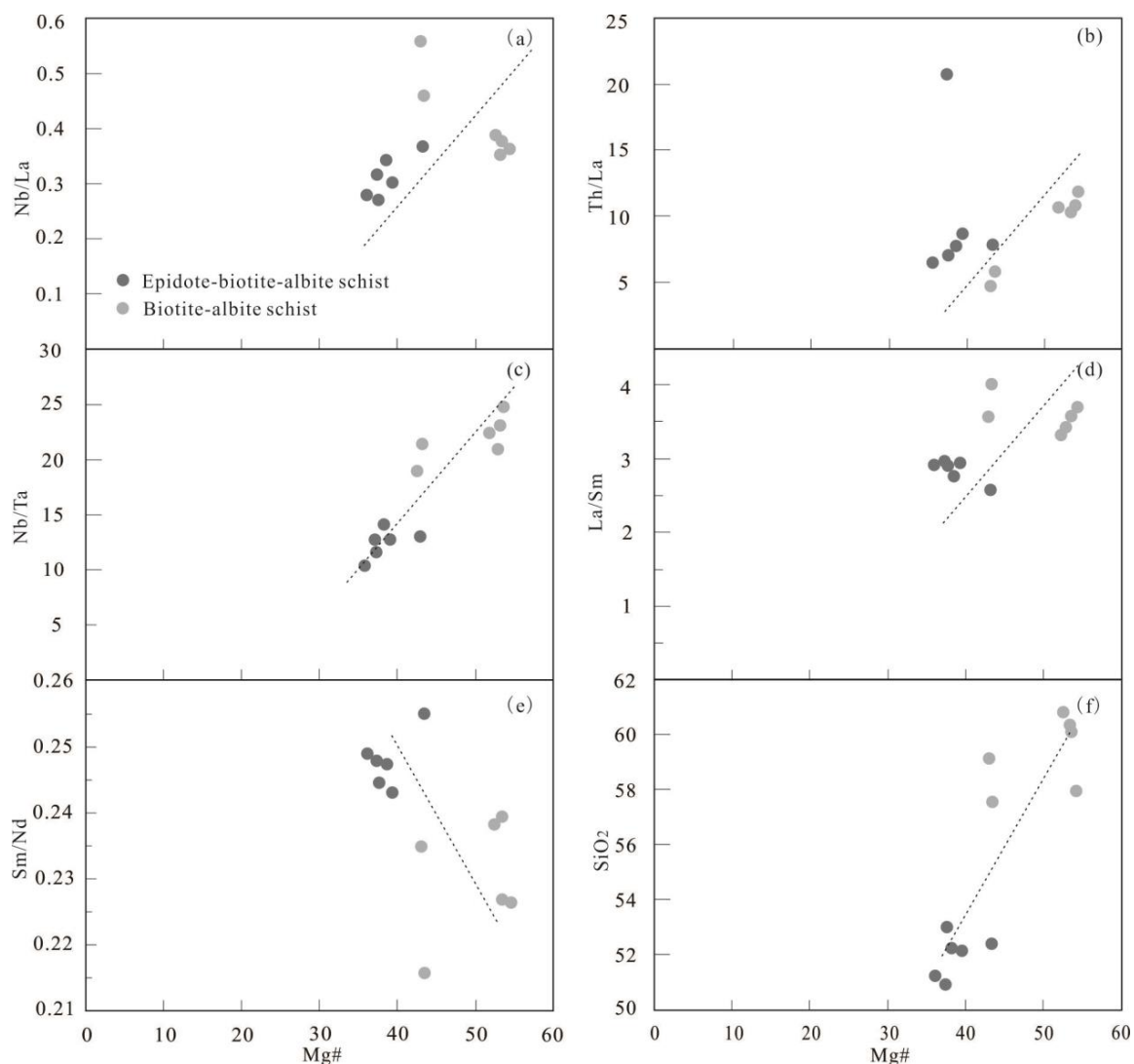


Figure 10. Plots of Nb/La vs. Mg# (a), Th/La vs. Mg# (b), Nb/Ta vs. Mg# (c), La/Sm vs. Mg# (d), Sm/Nd vs. Mg# (e) and SiO₂ vs. Mg# (f) for the Hadayang schists.

5.3.2. Fractional Crystallization

The Hadayang schists had low Mg# (35.2–53.0), Cr (23.7–86.5 ppm), Ni (21.1–40.0 ppm) and Co (12.1–30.6 ppm) contents relative to primitive-mantle-derived magmas, suggesting that our samples were evolved magmas rather than primitive magmas. The negative

correlation between Mg# and CaO and FeO^T , and the fact that Mg# was positively correlated with Cr, Ni, SiO_2 and Na_2O , indicated olivine and clinopyroxene fractionation (Figure 11). Based on the negative Eu anomalies, plagioclase fractionation also must have played an important role in the evolution of these magmas.

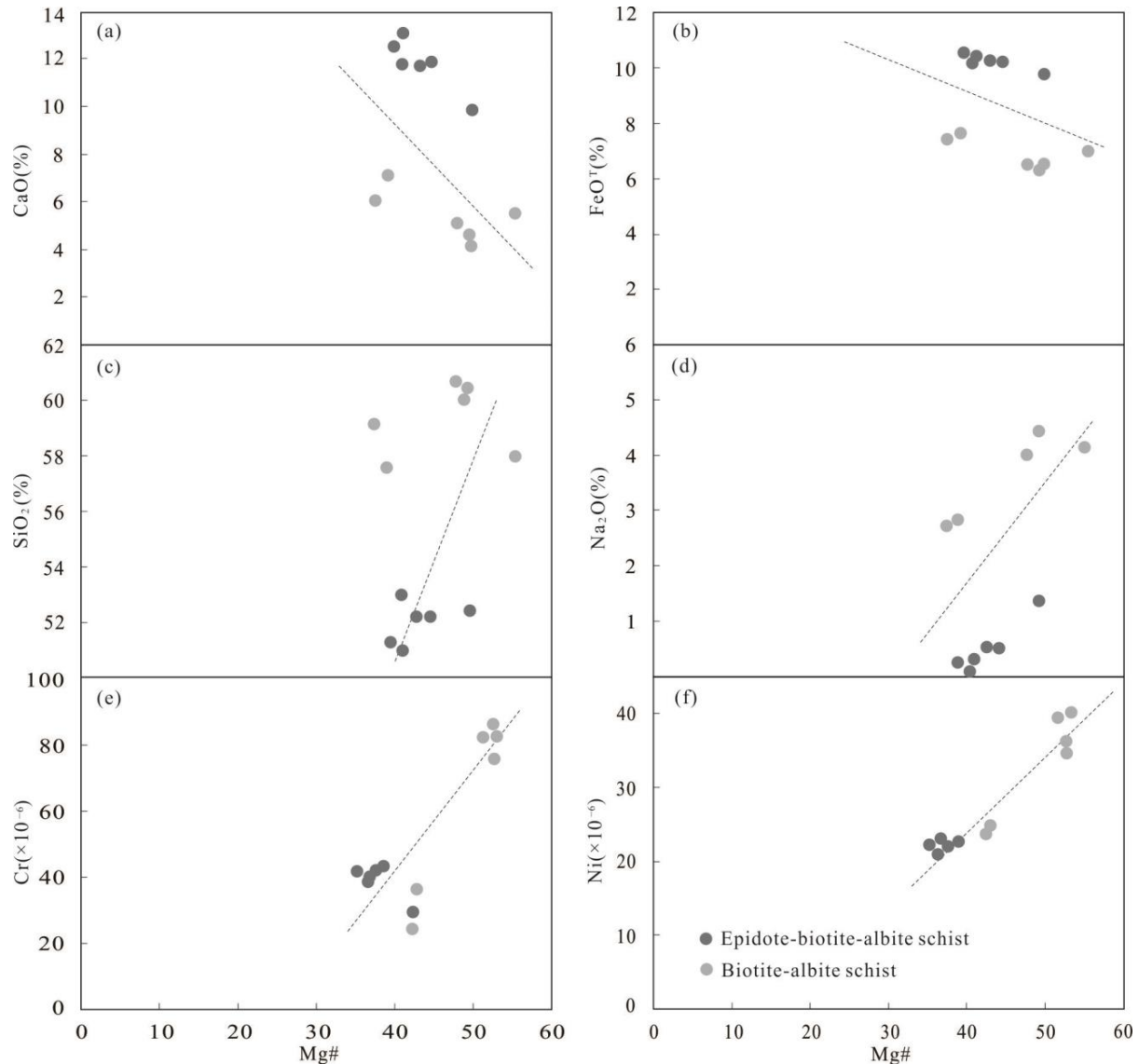


Figure 11. Plots of CaO vs. Mg# (a), FeO^T vs. Mg# (b), SiO_2 vs. Mg# (c), Na_2O vs. Mg# (d), Cr vs. Mg# (e) and Ni vs. Mg# (f) for the Hadayang schists.

5.3.3. Magma Source

The source region of basic volcanic rocks is generally asthenosphere or lithospheric mantle [92]. The low silica and alkali contents of the Hadayang schists, and their high MgO, Ti, Co and Cr contents, all favor a mantle magmatic source. This conclusion is also supported by the positive $\varepsilon_{\text{Hf}}(t)$ values (the average values were +8.93 and +9.29, respectively) (Figure 8). The T_{DMI} ages (552 to 781 Ma and 547 to 679 Ma, respectively) indicated that their parental magma fractionated from mantle in the Neoproterozoic period. As mentioned above, the Hadayang schists have LILE enrichment and significant HFSE depletion with moderately fractionated REE patterns and relatively low HREE abundances, suggesting that the components of the magma source may have included aqueous fluids released by dehydration of the subducted oceanic plate and/or partial melts derived from the subducted oceanic crust/sediments. The Ba/Th ratio of the Hadayang schist

samples varied significantly, while the $(\text{La}/\text{Sm})_{\text{N}}$ ratio was relatively constant (Figure 12b), indicating that fluids played a key role in the enrichment process, and the influence of sediment was small or absent. The wide range of the Sr/Nd (10.1–30.7) ratio values further indicated that fluid action played a major role in the process of mantle-derived magma enrichment. The above characteristics are supported by the Nb/Zr vs. Th/Zr plot (Figure 12a). The abundances and ratios of REEs are widely used to distinguish the source regions of magma and the degree of partial melting [93]. As can be seen in Sm/Yb vs. Sm and Sm/Yb vs. La/Yb plots (Figure 12c, d), the Hadayang schist samples plot mainly near or slightly deviating from the garnet + spinel lherzolite melting curves, and they fall between these two melting curves with starting compositions of primitive mantle, implying a mantle source consisting of spinel and garnet lherzolite, and that it took 1%–5% partial melting of this mantle source to produce the parent magma of the Hadayang schists (Figure 12c,d).

5.4. Tectonic Evolution and Geological Significance

Although a lot of progress has been made in the study of Late Devonian–Early Carboniferous magmatic rocks in the XB, there are still major disputes about their tectonic setting, including the active continental margin or island arc [16,58,59,79,82,83,86,87], back-arc basin [61,88], post-collision extensional [60] and subduction-related extension environment [78,81]. Some authors also believe that there was a transition from passive continental margin to island arc environment during this period [84,94]. In the following discussion, we suggest that the Late Devonian–Early Carboniferous magmatic rocks were formed in an intracontinental extension setting.

As mentioned in an earlier section, the Hadayang schists were characterized by LILE enrichment and significant HFSE depletion, and also exhibited moderately fractionated REE patterns and relatively low HREE abundances, which is also seen in the Late Devonian to Early Carboniferous basic magmatic rocks of the XB [61,78,86,88]. These geochemical characteristics are similar to those arc-type magmatic rocks [98], but there is some uncertainty in judging whether basic igneous rocks are arc magmatic rocks [99–101]. Previous studies have shown that the participation of fluids can change the geochemical characteristics of trace elements, and the precipitation of water-bearing fluid from subducting plates, or the release of water-bearing fluid from deep fluid circulation under the background of subducting plates, may lead to water-rich fluid metasomatism in the mantle source region, forming arc-like trace element characteristics [101–103]. Due to the differences in the contents of Zr, Ti and Sr elements between arc-like basalts and arc basalts, it is very effective to distinguish the two types of basalts by using a discriminant diagram of the above three elements [101]. On the plots of Ti/1000 vs. V, Zr vs. Zr/Y and Zr vs. Ti (Figure 13a,b,d), all of the Late Devonian to Early Carboniferous intermediate-basic magmatic rocks in the XB plot in the intraplate basalt field or deviating from the arc basalt area, similar to the geochemical characteristics of the North American Basin and Range basalt. As can be seen from the plot of Zr/Sm-Sr/Nd-Ti/V (Figure 13c), most of the samples plot in or near the intraplate magma and Basin and Range regions, which is significantly different from the nearly vertical characteristics of arc basalt. Based on the above analysis, we propose that the Late Devonian–Early Carboniferous intermediate-basic magmatic rocks in the eastern XB may have been formed in an intracontinental extension tectonic setting similar to the North American Basin and Range basalt. Coincidentally, the same tectonic background also appears in the western part of the XB. Previous studies have shown that the Erenhot–Hegenshan ophiolite in the XB was formed during the Late Devonian–Early Carboniferous [104–110] and was the product of the upwelling process of the asthenosphere caused by the extension of the lithosphere [111,112]. Based on the identification of basement rocks and other evidence around the ophiolite [113], it was indicated that the ophiolite would have been formed in the continental crust extension zone [6,114]. In summary, we believe that the XB would have been in the stage of intracontinental extension during the Late Devonian–Early Carboniferous.

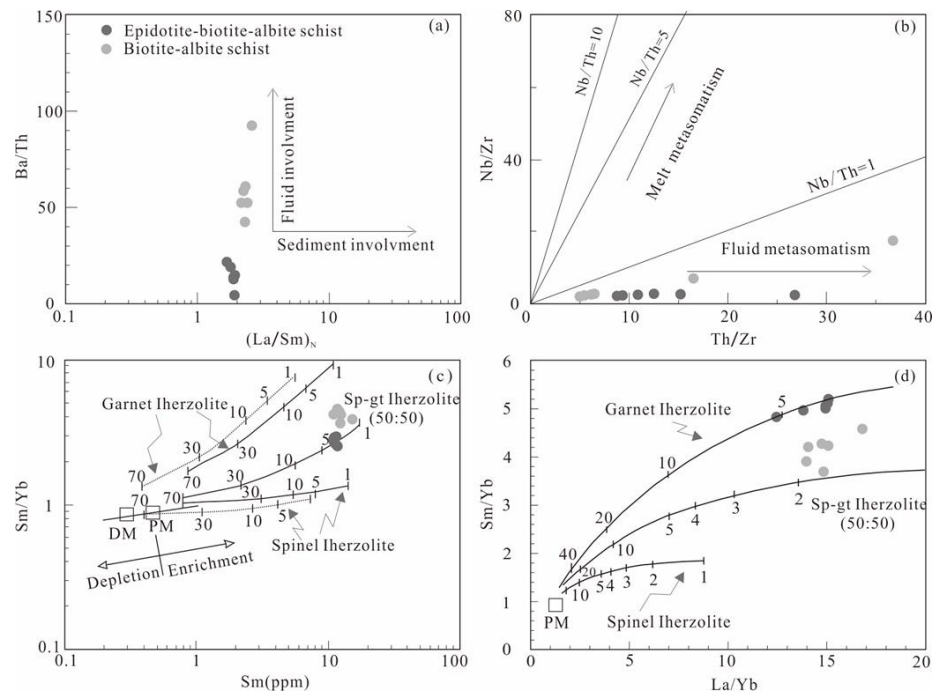


Figure 12. Plots of Nb/Zr vs. Th/Zr ((a), after [95]), La/Sm vs. Sm/Yb ((b), after [96]), Sm vs. Sm/Yb ((c), after [97]) and La/Yb vs. Sm/Yb ((d), after [97]) for the Hadayang schists.

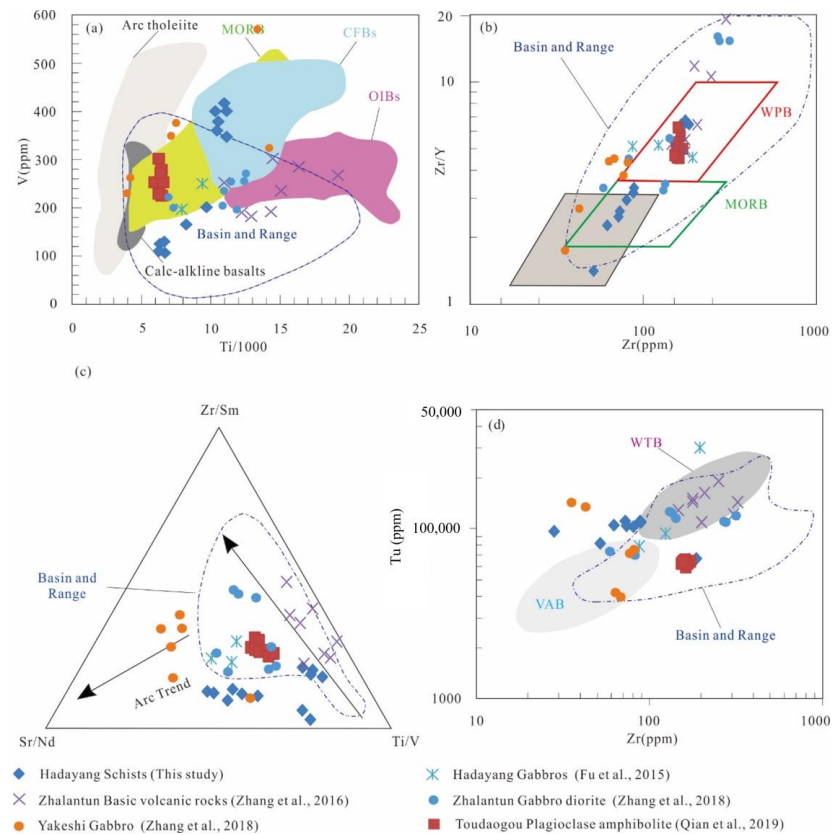


Figure 13. Structural discrimination diagrams of V vs. Ti/1000 ((a), after [115]), Zr/Y vs. Zr ((b), after [89]), Zr/Sm-Sr/Nd-Ti/V (c) and Ti vs. Zr ((d), after [116]) for Late Devonian to Early Carboniferous intermediate-basic rocks in the eastern XB. CFB = continental flood basalts; OIBs = ocean-island basalts; MORB = mid-ocean ridge basalt; WPB = within-plate basalts; IAB = island arc basalts; VAB = volcanic arc basalt; WTB = within-plate tholeiitic basalt.

6. Conclusions

1. The protolith of the Hadayang schists was intermediate-basic volcanic rock. LA-ICP-MS U-Pb dating of zircons from the epidote-biotite-albite schist and biotite-albite schist yielded crystallization ages of 360 ± 2 Ma (MSWD = 1.4) and 355 ± 3 Ma (MSWD = 2.1). This, combined with the presence of contemporaneous magmatic rocks in the region, indicates an important magmatic event in the eastern XB during the Late Devonian–Early Carboniferous.
2. The magma source of the Hadayang schists was a mantle that consisted of both spinel and garnet lherzolite, with a partial melting degree of 1%–5%, and which underwent fractional crystallization of olivine, orthopyroxene and plagioclase.
3. The Late Devonian–Early Carboniferous intermediate-basic magmatic rocks in the eastern XB were formed in an intracontinental extension setting, which is consistent with the tectonic setting of contemporaneous ophiolites in the western section. The Xing'an block would have been in the stage of intracontinental extension during the Late Devonian–Early Carboniferous.

Author Contributions: Conceptualization, F.N. and W.S. (Weimin Song); methodology, J.F.; software, Y.L.; validation, Y.W. and W.S. (Wei Sun); formal analysis, F.N.; investigation, J.F.; resources, J.F.; data curation, Y.L.; writing—original draft preparation, F.N. and W.S. (Weimin Song); writing—review and editing, Y.L. and J.F.; visualization, Y.W. and W.S. (Wei Sun); supervision, F.N.; project administration, J.F.; funding acquisition, W.S. (Weimin Song) and J.F. All authors have read and agreed to the published version of the manuscript.

Funding: This research was funded by the Geological Survey Project of China (Grant No. DD20230224 and DD20190360).

Data Availability Statement: The authors confirm that the data generated or analyzed during this study are provided in full within the published article.

Conflicts of Interest: The authors declare no conflict of interest.

References

1. Şengör, A.; Natal'in, B.; Burtman, V. Evolution of the Altaid tectonic collage and Palaeozoic crustal growth in Eurasia. *Nature* **1993**, *364*, 299–307. [[CrossRef](#)]
2. Jahn, B.-M.; Griffin, W.; Windley, B. Continental growth in the Phanerozoic: Evidence from Central Asia. *Tectonophysics* **2000**, *328*, 7–10. [[CrossRef](#)]
3. Jahn, B.-M. The Central Asian Orogenic Belt and growth of the continental crust in the Phanerozoic. *Geol. Soc. Lond. Spec. Publ.* **2004**, *226*, 73–100. [[CrossRef](#)]
4. Kröner, A.; Windley, B.; Badarch, G.; Tomurtogoo, O.; Hegner, E.; Jahn, B.M.; Gruschka, S.; Khain, E.V.; Demoux, A.; Wingate, M.T.D.; et al. Accretionary growth and crust formation in the Central Asian Orogenic Belt and comparison with the Arabian-Nubian shield. *Geol. Soc. Am. Mem.* **2007**, *200*, 461. [[CrossRef](#)]
5. Windley, B.F.; Alexeiev, D.; Xiao, W.; Kröner, A.; Badarch, G. Tectonic models for accretion of the Central Asian Orogenic Belt. *J. Geol. Soc.* **2007**, *164*, 31–47. [[CrossRef](#)]
6. Xu, B.; Zhao, P.; Bao, Q.Z.; Zhou, Y.H.; Wang, Y.Y.; Luo, Z.W. Preliminary study on the pre-Mesozoic tectonic unit division of the Xing-Meng Orogenic Belt (XMOB). *Acta Petrol. Sin.* **2014**, *30*, 1841–1857, (In Chinese with English Abstract).
7. Xu, B.; Zhao, P.; Wang, Y.Y.; Liao, W.; Luo, Z.W.; Bao, Q.Z.; Zhou, Y.H. The pre-Devonian tectonic framework of Xing'an–Mongolia orogenic belt (XMOB) in north China. *J. Asian Earth Sci.* **2015**, *97*, 183–196. [[CrossRef](#)]
8. Liu, Y.; Li, W.; Feng, Z.; Wen, Q.; Neubauer, F.; Liang, C. A review of the Paleozoic tectonics in the eastern part of Central Asian Orogenic Belt. *Gondwana Res.* **2017**, *43*, 123–148. [[CrossRef](#)]
9. Liu, Y.; Li, W.; Ma, Y.; Feng, Z.; Guan, Q.; Li, S.; Chen, Z.; Liang, C.; Wen, Q. An orocline in the eastern Central Asian Orogenic Belt. *Earth-Sci. Rev.* **2021**, *221*, 103808. [[CrossRef](#)]
10. Zhou, J.B.; Wilde, S.A.; Zhao, G.C.; Han, J. Nature and assembly of microcontinental blocks within the Paleo-Asian Ocean. *Earth-Sci. Rev.* **2018**, *186*, 76–93. [[CrossRef](#)]
11. Xu, W.L.; Sun, Y.C.; Tang, J.; Luan, J.P.; Wang, F. Basement nature and tectonic evolution of the Xing'an–Mongolian Orogenic belt. *Earth Sci.* **2019**, *44*, 1620–1646, (In Chinese with English Abstract). [[CrossRef](#)]
12. Zhang, J.M.; Xu, B.; Yan, L.J.; Wang, Y.Y. Evolution of the Heihe–Nenjiang Ocean in the eastern Paleo-Asian Ocean: Constraints of sedimentological, geochronological and geochemical investigations from Early–Middle Paleozoic Heihe–Dashizhai Orogenic Belt in the northeast China. *Gondwana Res.* **2020**, *81*, 339–361. [[CrossRef](#)]

13. Ma, Y.F. The Late Paleozoic Tectonic Evolution of the Central Great Xing'an Range, NE China. Ph.D. Thesis, Jilin University, Changchun, China, 2019. (In Chinese with English Abstract).
14. Ma, Y.-F.; Liu, Y.-J.; Wang, Y.; Qin, T.; Chen, H.J.; Sun, W.; Zang, Y.Q. Late Carboniferous mafic to felsic intrusive rocks in the central Great Xing'an Range, NE China: Petrogenesis and tectonic implications. *Int. J. Earth Sci.* **2020**, *109*, 761–783. [[CrossRef](#)]
15. Liu, Y.J.; Feng, Z.Q.; Jiang, L.W.; Jin, W.; Li, W.M.; Guan, Q.B.; Wen, Q.B.; Liang, C.Y. Ophiolite in the eastern Central Asian Orogenic Belt, NE China. *Acta Pet. Sin.* **2019**, *35*, 3017–3047, (In Chinese with English Abstract). [[CrossRef](#)]
16. Li, Y.; Xu, W.-L.; Tang, J.; Sun, C.-Y.; Zhang, X.-M.; Xiong, S. Late Paleozoic igneous rocks in the Xing'an Massif and its amalgamation with the Songnen Massif, NE China. *J. Asian Earth Sci.* **2020**, *197*, 104407. [[CrossRef](#)]
17. Shao, J.A. *Crust Evolution in the Middle Part of the Northern Margin of Sino-Korean Plate*; Peking University Press: Beijing, China, 1991; pp. 1–136, (In Chinese with English Abstract).
18. Hong, D.; Huang, H.; Xiao, Y.; Xu, H.; Jin, M. The Permian alkaline granites in Central Inner Mongolia and their geodynamic significance. *Acta Geol. Sin. Engl. Ed.* **1995**, *8*, 27–39. [[CrossRef](#)]
19. Sun, D.Y.; Wu, F.Y.; Li, H.M.; Lin, Q. Emplacement age of the postorogenic A-type granites in Northwestern Lesser Xing'an Ranges, and its relationship to the eastward extension of Suolushan-Hegenshan-Zhalaithe collisional suture zone. *Chin. Sci. Bull.* **2001**, *46*, 427–432. [[CrossRef](#)]
20. Tong, Y.; Hong, D.W.; Wang, T.; Shi, X.J.; Zhang, J.J.; Zeng, T. Spatial and temporal distribution of granitoids in the middle segment of the Sino-Mongolian Border and its tectonic and metallogenic implications. *Acta Geosci. Sin.* **2010**, *31*, 395–412, (In Chinese with English Abstract).
21. Chen, B.; Jahn, B.-M.; Wilde, S.; Xu, B. Two contrasting paleozoic magmatic belts in northern Inner Mongolia, China: Petrogenesis and tectonic implications. *Tectonophysics* **2000**, *328*, 157–182. [[CrossRef](#)]
22. Miao, L.C.; Fan, W.M.; Zhang, F.Q.; Liu, D.Y.; Jian, P.; Shi, G.H.; Tao, H.; Shi, Y.Q. Zircon SHRIMP geochronology of the Xinkailing-Kele complex in the northwestern Lesser Xing'an Range, and its geological implications. *Chin. Sci. Bull.* **2004**, *49*, 201–209. [[CrossRef](#)]
23. Yarmolyuk, V.V.; Kovalenko, V.I.; Sal'nikova, E.B.; Kovach, V.P.; Kozlovsky, A.M.; Kotov, A.B.; Lebedev, V.I. Geochronology of igneous rocks and formation of the Late Paleozoic south Mongolian active margin of the Siberian continent. *Strat. Geol. Correl.* **2008**, *162*, 162–181. [[CrossRef](#)]
24. Sun, L.X.; Ren, B.F.; Zhao, F.Q.; Ji, S.P.; Geng, J.Z. Late Paleoproterozoic magmatic records in the Erguna massif: Evidences from the zircon U-Pb dating of granitic gneisses. *Geol. Bull. China* **2013**, *32*, 341–352, (In Chinese with English Abstract). [[CrossRef](#)]
25. Shao, J.; Li, Y.F.; Zhou, Y.H.; Wang, H.B.; Zhang, J. Neo-Archaean magmatic event in Erguna Massif of northeast China: Evidence from the zircon LA-ICP-MS dating of the gneissic monogranite from the drill. *J. Jilin Univ. Earth Sci. Ed.* **2015**, *45*, 364–373, (In Chinese with English Abstract). [[CrossRef](#)]
26. Li, G.Y.; Zhou, J.B.; Li, L.; Han, J.; Song, M.C. Paleoproterozoic basement of the Xing'an Block in the eastern Central Asian Orogenic Belt: Evidence from the geochemistry and zircon U-Pb geochronology of granitic gneisses. *Precambrian Res.* **2019**, *331*, 105372. [[CrossRef](#)]
27. Feng, Z.Q.; Zhang, Q.H.; Liu, Y.J.; Li, L.; Jiang, L.W.; Zhou, J.P.; Li, W.M.; Ma, Y.F. Reconstruction of Rodinia supercontinent: Evidence from the Erguna Block (NE China) and adjacent units in the eastern Central Asian orogenic Belt. *Precambrian Res.* **2022**, *368*, 106467. [[CrossRef](#)]
28. Ge, W.C.; Chen, J.S.; Yang, H.; Zhao, G.C.; Zhang, Y.L.; Tian, D.X. Tectonic implications of new zircon U-Pb ages for the Xinghuadukou Complex, Erguna Massif, northern Great Xing'an Range, NE China. *J. Asian Earth Sci.* **2015**, *106*, 169–185. [[CrossRef](#)]
29. Zhao, S.; Xu, W.-L.; Tang, J.; Li, Y.; Guo, P. Timing of formation and tectonic nature of the purportedly Neoproterozoic Jiageda Formation of the Erguna Massif, NE China: Constraints from field geology and U-Pb geochronology of detrital and magmatic zircons. *Precambrian Res.* **2016**, *281*, 585–601. [[CrossRef](#)]
30. Xu, J.L.; Zheng, C.Q.; Tajčmanová, L.; Zhong, X.; Han, X.M.; Wang, Z.Y.; Yang, Y. Phase Equilibria Modeling and Zircon Dating for Precambrian Metapelites from the Xinghuadukou Complex in the Lulin Forest of the Erguna Massif, Northeast China. *J. Earth Sci.* **2018**, *29*, 1276–1290. [[CrossRef](#)]
31. Liu, H.C.; Li, Y.L.; Wan, Z.F.; Lai, C.K. Early Neoproterozoic tectonic evolution of the Erguna Terrane (NE China) and its paleogeographic location in Rodinia supercontinent: Insights from magmatic and sedimentary record. *Gondwana Res.* **2020**, *88*, 185–220. [[CrossRef](#)]
32. Tang, J.; Xu, W.L.; Wang, F.; Wang, W.; Xu, M.J.; Zhang, Y.H. Geochronology and geochemistry of Neoproterozoic magmatism in the Erguna Massif, NE China: Petrogenesis and implications for the breakup of the Rodinia supercontinent. *Precambrian Res.* **2013**, *244*, 597–615. [[CrossRef](#)]
33. Zhao, S.; Xu, W.L.; Wang, F.; Wang, W.; Tang, J.; Zhang, Y.H. Neoproterozoic Magmatism in the Erguna Massif, NE China: Evidence from Zircon U-Pb Geochronology. *Geotecton. Metallog.* **2016**, *40*, 559–573, (In Chinese with English Abstract). [[CrossRef](#)]
34. Zhao, S.; Xu, W.L.; Tang, J.; Li, Y.; Guo, Y.P. Neoproterozoic magmatic events and tectonic attribution of the Erguna Massif: Constraints from geochronological, geochemical and Hf isotopic data of intrusive rocks. *Earth Sci.* **2016**, *41*, 1803–1829, (In Chinese with English Abstract). [[CrossRef](#)]
35. Sun, W.; Chi, X.-G.; Zhao, Z.; Pan, S.-Y.; Liu, J.-F.; Zhang, R.; Quan, J.-Y. Zircon geochronology constraints on the age and nature of 'Precambrian metamorphic rocks' in the Xing'an block of Northeast China. *Int. Geol. Rev.* **2014**, *56*, 672–694. [[CrossRef](#)]

36. Na, F.C.; Song, W.M.; Liu, Y.C.; Wang, Y.; Fu, J.Y.; Sun, W.; Li, L.C.; Wu, J.W.; Ge, J.T.; Tan, H.Y. Chronological study and tectonic significance of Precambrian metamorphic rocks in Zhalantun area of Da Hinggan Mountains. *Geol. Bull. China* **2018**, *37*, 1607–1619, (In Chinese with English Abstract).
37. Na, F.C.; Fu, J.Y.; Song, W.M.; Liu, Y.C.; Wang, Y.; Ge, J.T.; Sun, W.; Yang, F.; Zhang, G.Y.; Zhong, H. Petrological and geochronological study of Keluo Complex in northwestern Lesser Xing'an Range. *Earth Sci.* **2019**, *44*, 3265–3278, (In Chinese with English Abstract) [[CrossRef](#)]
38. Zhang, C.; Wu, X.; Guo, W.; Zhang, Y.; Quan, J. Discovery of the 1.8 Ga Granite on the Western Margin of the Songnen Massif, China. *Acta Geol. Sin. Engl. Ed.* **2017**, *91*, 1497–1498. [[CrossRef](#)]
39. Zhang, C.; Wu, X.W.; Liu, Z.H.; Zhang, Y.J.; Guo, W.; Quan, J.Y. Precambrian geological events on the western margin of Songnen massif: Evidence from LA-ICP-MS U-Pb geochronology of zircons from Paleoproterozoic granite in the Longjiang area. *Acta Petrol. Sin.* **2018**, *34*, 3137–3152, (In Chinese with English Abstract) [[CrossRef](#)]
40. Qian, C.; Chen, H.J.; Lu, L.; Pang, X.J.; Qin, T.; Wang, Y. The discovery of Neoproterozoic granite in Longjiang area, Heilongjiang Province. *Acta Geosci. Sin.* **2018**, *39*, 27–36, (In Chinese with English Abstract) [[CrossRef](#)]
41. Wu, X.W.; Zhang, C.; Zhang, Y.J.; Guo, W.; Zhang, C.; Cui, T.R.; Yang, Y.J.; Hu, J.F.; Song, W.B. 2.7 Ga Monzogranite on the Songnen Massif and Its Geological Implications. *Acta Geol. Sin. Engl. Ed.* **2018**, *92*, 1265–1266. [[CrossRef](#)]
42. Wu, X.W.; Zhang, C.; Shao, J.; Guo, W.; Li, L.C.; Zhang, G.Y.; Liu, B.S.; Song, W.B. The Neoproterozoic to Paleoproterozoic magmatic events in Longjiang area and Ulanhot area: Constraint on the attribute of Precambrian geological units in western Songnen massif. *Acta Petrol. Sin.* **2022**, *38*, 2811–2828, (In Chinese with English Abstract)
43. Cheng, Z.X.; Wang, Y.; Qian, C.; Yang, X.P.; Li, Z.H.; Liu, H.W.; Xiao, L. The discovery of the Paleoproterozoic metamorphic rocks in Ulanhot, Inner Mongolia, and its geological significance. *Geol. Bull. China* **2018**, *37*, 1599–1606, (In Chinese with English Abstract)
44. Zhao, P.; Fang, J.Q.; Xu, B.; Chen, Y.; Faure, M. Early Paleozoic tectonic evolution of the Xing-Meng Orogenic Belt: Constraints from detrital zircon geochronology of western Erguna–Xing'an Block, North China. *J. Asian Earth Sci.* **2014**, *95*, 136–146. [[CrossRef](#)]
45. Zhou, J.B.; Wang, B.; Wilde, S.A.; Zhao, G.C.; Cao, J.L.; Zheng, C.Q. Geochemistry and U–Pb zircon dating of the Toudaoqiao blueschists in the Great Xing'an Range, northeast China, and tectonic implications. *J. Asian Earth Sci.* **2015**, *97*, 197–210. [[CrossRef](#)]
46. Miao, L.C.; Zhang, F.C.; Jiao, S.J. Age, protoliths and tectonic implications of the Toudaoqiao blueschist, Inner Mongolia, China. *J. Asian Earth Sci.* **2015**, *105*, 360–373. [[CrossRef](#)]
47. Zhao, L.M.; Takasu, A.; Liu, Y.J.; Li, W.M. Blueschist from the Toudaoqiao Area, Inner Mongolia, NE China: Evidence for the Suture between the Ergun and the Xing'an Blocks. *J. Earth Sci.* **2017**, *28*, 241–248. [[CrossRef](#)]
48. Feng, Z.Q.; Liu, Y.J.; Li, Y.R.; Li, W.M.; Wen, Q.B.; Liu, B.Q.; Zhou, J.P.; Zhao, Y.L. Ages, geochemistry and tectonic implications of the Cambrian igneous rocks in the northern Great Xing'an Range, NE China. *J. Asian Earth Sci.* **2017**, *144*, 5–21. [[CrossRef](#)]
49. Feng, Z.Q.; Liu, Y.J.; Li, L.; She, H.Q.; Jiang, L.W.; Du, B.Y.; Liu, Y.W.; Li, W.M.; Wen, Q.B.; Liang, C.Y. Subduction, accretion, and collision during the Neoproterozoic–Cambrian orogeny in the Great Xing'an Range, NE China: Insights from geochemistry and geochronology of the Ali River ophiolitic mélange and arc-type granodiorites. *Precambrian Res.* **2018**, *311*, 117–135. [[CrossRef](#)]
50. Gao, F.H.; Wang, F.; Xu, W.L.; Yang, Y. Age of the “Paleoproterozoic” Dongfengshan Group in the Lesser Xing'an Range, NE China, and its tectonic implications: Constraints from zircon U–Pb geochronology. *J. Jilin Univ. Earth Sci. Ed.* **2013**, *43*, 440–456, (In Chinese with English Abstract). [[CrossRef](#)]
51. Quan, J.Y.; Chi, X.G.; Zhang, R.; Fan, L.F.; Hu, Z.C. LA-ICP-MS U–Pb geochronology of detrital zircon from the Neoproterozoic Dongfengshan Group in Songnen massif and its geological significance. *Geol. Bull. China* **2013**, *32*, 353–364, (In Chinese with English Abstract). [[CrossRef](#)]
52. Wang, F.; Xu, W.L.; Gao, F.H.; Zhang, H.H.; Pei, F.P.; Zhao, L.; Yang, Y. Precambrian terrane within the Songnen–Zhangguangcai Range Massif, NE China: Evidence from U–Pb ages of detrital zircons from the Dongfengshan and Tadong groups. *Gondwana Res.* **2014**, *26*, 402–413. [[CrossRef](#)]
53. Luan, J.P.; Xu, W.L.; Wang, F.; Wang, Z.W.; Guo, P. Age and geochemistry of Neoproterozoic granitoids in the Songnen–Zhangguangcai Range Massif, NE China: Petrogenesis and tectonic implications. *J. Asian Earth Sci.* **2017**, *148*, 265–276. [[CrossRef](#)]
54. Luan, J.P.; Yu, J.J.; Yu, J.L.; Cui, Y.C.; Xu, W.L. Early Neoproterozoic magmatism and the associated metamorphism in the Songnen Massif, NE China: Petrogenesis and tectonic implications. *Precambrian Res.* **2019**, *328*, 250–268. [[CrossRef](#)]
55. Luan, J.P.; Tang, J.; Xu, W.L.; Guo, P.; Long, X.Y.; Xiong, S. Petrogenesis of Neoproterozoic magmatic rocks in the Songnen Massif (northeastern China): Implications for basement composition and crustal growth. *Precambrian Res.* **2022**, *376*, 106687. [[CrossRef](#)]
56. Zhang, L.Y.; Wang, Z.W.; Xu, B.; Zou, H.B.; Zhao, P.; Zhang, H. Neoproterozoic–Early Cambrian igneous and sedimentary sequences in the Songliao Block, NE China: Records of Rodinia supercontinent evolution in eastern Central Asian orogenic Belt. *Precambrian Res.* **2022**, *381*, 106865. [[CrossRef](#)]
57. Na, F.C.; Fu, J.Y.; Wang, Y.; Yang, F.; Zhang, G.Y.; Liu, Y.C.; Kang, Z. LA-ICP-MS zircon U–Pb age of the chlorite-muscovite tectonic schist in Hadayang, Morin Dawa Banner, Inner Mongolia, and its tectonic significance. *Geol. Bull. China* **2014**, *33*, 1326–1332, (In Chinese with English Abstract). [[CrossRef](#)]
58. Zhao, Z.; Chi, X.G.; Pan, S.Y.; Liu, J.F.; Sun, W.; Hu, Z.C. Zircon U–Pb LA-ICP-MS dating of Carboniferous volcanics and its geological significance in the northwestern Lesser Xing'an Range. *Acta Petrol. Sin.* **2010**, *26*, 2452–2464, (In Chinese with English Abstract)

59. Feng, Z.Q.; Li, W.M.; Liu, Y.J.; Jin, W.; Wen, Q.B.; Liu, B.Q.; Zhou, J.P.; Zhang, T.A.; Li, X.Y. Early Carboniferous tectonic evolution of the northern Heihe-Nenjiang-Hegenshan suture zone, NE China: Constraints from the mylonitized Nenjiang rhyolites and the Moguqi gabbros. *Geol. J.* **2018**, *53*, 1005–1021. [\[CrossRef\]](#)
60. Yang, F.; Na, F.C.; Zhang, G.Y.; Wang, Y.; Fu, J.Y.; Sun, W.; Chen, J.S.; Li, B.; Liu, M.; Pang, X.J.; et al. New Discovery of the Devonian Orthoclase Granite of Nenjiang-Heihe Structural belt, China and its Zircon U-Pb Data. *Acta Geol. Sin. Engl. Ed.* **2018**, *92*, 874–875. [\[CrossRef\]](#)
61. Fu, J.Y.; Wang, Y.; Na, F.C.; Sun, W.; Yang, F.; Zhong, H.; Zhang, G.Y.; Liu, Y.C. Zircon U-Pb geochronology and geochemistry of the Hadayang mafic-ultramafic rocks in Inner Mongolia: Constraints on the Late Devonian subduction of Nenjiang-Heihe area, Northeast China. *Geol. China* **2015**, *42*, 1740–1753, (In Chinese with English Abstract).
62. Fu, J.Y.; Wang, Y.; Na, F.C.; Zhang, G.Y.; Liu, Y.C.; Kang, Z. Geology of the Hadayang tectonic mélange in Inner Mongolia: Discovery significance. *Geol. Resour.* **2015**, *24*, 408–413, (In Chinese with English Abstract). [\[CrossRef\]](#)
63. Hou, K.J.; Li, Y.H.; Tian, Y.R. In situ U-Pb zircon dating using laser ablation-multiion counting-ICP-MS. *Miner. Depos.* **2009**, *28*, 481–492, (In Chinese with English Abstract). [\[CrossRef\]](#)
64. Liu, Y.S.; Gao, S.; Hu, Z.C.; Gao, C.G.; Zong, K.Q.; Wang, D.B. Continental and oceanic crust recycling-induced melt-peridotite interactions in the Trans-North China Orogen: U-Pb dating, Hf isotopes and trace elements in zircons from mantle xenoliths. *J. Pet.* **2010**, *51*, 537–571. [\[CrossRef\]](#)
65. Sláma, J.; Kosler, J.; Condon, D.J.; Crowley, J.L.; Gerdes, A.; Hanchar, J.M.; Horstwood, M.S.A.; Morris, G.A.; Nasdala, L.; Norberg, N.; et al. Plešovice zircon—A new natural reference material for U–Pb and Hf isotopic microanalysis. *Chem. Geol.* **2008**, *249*, 1–35. [\[CrossRef\]](#)
66. Hou, K.J.; Yanhe, L.I.; Xie, G.Q. Laser ablation-MC-ICP-MS technique for Hf isotope microanalysis of zircon and its geological applications. *Acta Petrol. Sin.* **2007**, *23*, 2595–2604, (In Chinese with English Abstract). [\[CrossRef\]](#)
67. Le Maitre, R.W.; Streckeisen, A.; Zanettin, B.; Bas, M.J.L.; Bonin, B.; Bateman, P. *Igneous Rocks: A Classification and Glossary of Terms*; Cambridge University Press: Cambridge, UK, 2005; p. 256.
68. Irvine, T.N.; Baragar, W.R.A. A Guide to the chemical classification of the common volcanic rocks. *Can. J. Earth Sci.* **1971**, *8*, 523–548. [\[CrossRef\]](#)
69. Winchester, J.A.; Floyd, P.A. Geochemical discrimination of different magma series and their differentiation products using immobile elements. *Chem. Geol.* **1977**, *20*, 325–343. [\[CrossRef\]](#)
70. Miyashiro, A. Volcanic rock series in island arcs and active continental margins. *Am. J. Sci.* **1974**, *274*, 321–355. [\[CrossRef\]](#)
71. Boynton, W.V. Cosmochemistry of the Rare Earth Elements: Meteorite Studies. *Dev. Geochem.* **1984**, *2*, 63–114. [\[CrossRef\]](#)
72. Sun, S.S.; McDonough, W.F. Chemical and isotopic systematics of oceanic basalts: Implications for mantle composition and processes. *Geol. Soc. Lond.* **1989**, *42*, 313–345. [\[CrossRef\]](#)
73. Rubatto, D.; Gebauer, D. Use of cathodoluminescence for U-Pb Zircon dating by Ion Microprobe: Some examples from the western Alps. In *Cathodoluminescence in Geoscience*; Springer: Berlin/Heidelberg, Germany, 2000; pp. 373–400. [\[CrossRef\]](#)
74. Wu, J.S.; Geng, Y.S.; Xu, H.F.; Jin, L.G.; He, S.Y.; Sun, S.W. Metamorphic geology of the Fuping Group. *Bull. Inst. Geol. Chin. Acad. Geol. Sci.* **1989**, *19*, 231. (In Chinese)
75. Simonen, A. Stratigraphy and sedimentation of the Svecofennidie, Early Archean supracrustal rocks in southwestern Finland. *Bull. Geol. Soc. Finl.* **1953**, *160*, 1–64.
76. Heilongjiang Bureau of Geology and Mineral Resources (HBGMR). *Regional Geology of Heilongjiang Province*; Geological Publishing House: Beijing, China, 1993; pp. 57–734, (In Chinese with English Abstract).
77. Wu, F.Y.; Sun, D.Y.; Ge, W.C.; Zhang, Y.B.; Grant, M.L.; Wende, S.A.; Jahn, B.M. Geochronology of the Phanerozoic granitoids in northeastern China. *J. Asian Earth Sci.* **2011**, *41*, 1–30. [\[CrossRef\]](#)
78. Zhang, Y.; Pei, F.P.; Wang, Z.W.; Xu, W.L.; Li, Y.; Wang, F.; Zhou, Z.B. Late Paleozoic tectonic evolution of the central Great Xing’an Range, northeast China: Geochronological and geochemical evidence from igneous rocks. *Geol. J.* **2018**, *53*, 282–303. [\[CrossRef\]](#)
79. Zhao, Z.; Chi, X.G.; Liu, J.F.; Wang, T.F.; Hu, Z.C. Late Paleozoic arc-related magmatism in Yakeshi region, Inner Mongolia: Chronological and geochemical evidence. *Acta Petrol. Sin.* **2010**, *26*, 3245–3258, (In Chinese with English Abstract).
80. She, H.Q.; Li, J.W.; Xiang, A.P.; Guan, J.D.; Yang, X.C.; Zhang, D.Q.; Tan, G.; Zhang, B. U-Pb ages of the zircons from primary rocks in middle-northern Daxinganling and its implications to geotectonic evolution. *Acta Petrol. Sin.* **2012**, *28*, 571–594, (In Chinese with English Abstract).
81. Ji, Z.; Ge, W.C.; Yang, H.; Zhang, Y.L.; Dong, Y.; Bi, J.H.; Liu, X.W. Geochronology and geochemistry of Late Devonian I- and A-Type granites from the Xing’an Block, NE China: Implications for slab break-off during subduction of the Hegenshan-Heihe Ocean. *J. Earth Sci.* **2022**, *33*, 150–160. [\[CrossRef\]](#)
82. Shi, L.; Zheng, Z.Q.; Yao, W.G.; Li, J.; Cui, F.H.; Gao, F.; Gao, Y.; Xu, J.L. Geochronological framework and tectonic setting of the granitic magmatism in the Chaihe–Moguqi region, central Great Xing’an Range, China. *J. Asian Earth Sci.* **2015**, *113*, 443–453. [\[CrossRef\]](#)
83. Qian, C.; Lu, L.; Qin, T.; Li, L.C.; Chen, H.J.; Cui, T.R.; Jiang, B.; Na, F.C.; Sun, W.; Wang, Y.; et al. The Early Late-Paleozoic granitic magmatism in the Zhalantun region, Northern Great Xing’an range, NE China: Constraints on the timing of amalgamation of Erguna-Xing’an and Songnen Blocks. *Acta Geol. Sin.* **2018**, *92*, 2706–2720, (In Chinese with English Abstract). [\[CrossRef\]](#)

84. Ma, Y.F.; Liu, Y.J.; Qin, T.; Sun, W.; Zang, Y.L.; Zhang, Y.J. Late Devonian to early Carboniferous magmatism in the western Songliao–Xinlinhot block, Northeast China: Implications for eastward subduction of the Nenjiang oceanic lithosphere. *Geol. J.* **2020**, *55*, 2208–2231. [[CrossRef](#)]
85. Li, D.X.; Zheng, C.Q.; Liang, C.Y.; Zhou, X.; Yang, Y.; Song, Z.W.; Chen, L.; Geng, Z.Z.; Zhao, Y.L. Genesis and Geological Significance of Granitic Mylonites in Southern Zhalantun, Central Xing’an Range. *Earth Sci.* **2022**, *47*, 3354–3370, (In Chinese with English Abstract). [[CrossRef](#)]
86. Zhang, Y.J.; Zhang, C.; Wu, X.W.; Cui, T.R.; Yang, Y.J.; Chen, H.J.; Jiang, B.; Guo, W.; Ma, Y.F. Geochronology and geochemistry of Late Paleozoic marine volcanic from the Zhalanun area in Northern DaHingan Mountains and its geological significance. *Acta Geol. Sin.* **2016**, *90*, 2706–2720, (In Chinese with English Abstract) [[CrossRef](#)]
87. Yang, B.; Zhang, B.; Zhang, Q.K.; Ma, W.; Zhao, M.T.; Chen, S.L.; Yuan, X. Characteristics and geological significance of Early Carboniferous high-Mg andesites in Ma’anshan area, east Inner Mongolia. *Geol. Bull. China* **2018**, *37*, 1760–1771, (In Chinese with English Abstract)
88. Qian, C.; Wang, Y.; Lu, L.; Qin, T.; Li, L.C.; Cui, T.R.; Chen, H.J.; Yang, L. Geochronology, geochemistry and Hf isotopic composition of amphibolite from Zhalantun region in northern Great Xing’an Range and its tectonic significance. *Earth Sci.* **2019**, *44*, 3193–3208, (In Chinese with English Abstract) [[CrossRef](#)]
89. Pearce, J.; Norry, M. Petrogenetic implications of Ti, Zr, Y, and Nb variations in volcanic rocks. *Contrib. Miner. Pet.* **1979**, *69*, 33–47. [[CrossRef](#)]
90. DePaolo, D.C. Trace element and isotopic effects of combined wallrock assimilation and fractional crystallization. *Earth Planet. Sci. Lett.* **1981**, *53*, 189–202. [[CrossRef](#)]
91. Wang, X.C.; Li, Z.X.; Li, X.H.; Li, J.; Xu, Y.G.; Li, X.H. Identification of an ancient mantle reservoir and young recycled materials in the source region of a young mantle plume: Implications for potential linkages between plume and plate tectonics. *Earth Planet. Sci. Lett.* **2013**, *377–378*, 248–259. [[CrossRef](#)]
92. Zhang, H.-F.; Sun, M.; Zhou, X.-H.; Ying, J.-F. Geochemical constraints on the origin of Mesozoic alkaline intrusive complexes from the North China Craton and tectonic implications. *Lithos* **2005**, *81*, 297–317. [[CrossRef](#)]
93. Dilek, Y.; Furnes, H. Ophiolite genesis and global tectonics: Geochemical and tectonic fingerprinting of ancient oceanic lithosphere. *Geol. Soc. Am. Bull.* **2011**, *123*, 387–411. [[CrossRef](#)]
94. Ma, Y.F.; Liu, Y.J.; Wang, Y.; Tang, Z.; Qian, C.; Qin, T.; Feng, Z.Q.; Sun, W.; Zang, Y.Q. Geochronology and geochemistry of the Carboniferous felsic rocks in the central Great Xing’an Range, NE China: Implications for the amalgamation history of Xing’an and Songliao–Xinlinhot blocks. *Geol. J.* **2019**, *54*, 482–513. [[CrossRef](#)]
95. Elliott, T. Tracers of the slab. In *Inside the Subduction Factory*; Eiler, J., Ed.; AGU: Washington, DC, USA, 2003; pp. 23–45. [[CrossRef](#)]
96. Kepezhinskas, P.; McDermott, F.; Defant, M.J.; Hochstaedter, A.; Drummond, M.S.; Hawkesworth, C.J.; Koloskov, A.; Maury, R.C.; Bellon, H. Trace element and Sr-Nd-Pb isotopic constraints on a three-component model of Kamchatka Arc petrogenesis. *Geochim. Cosmochim. Acta* **1997**, *61*, 577–600. [[CrossRef](#)]
97. Aldanmaz, E.; Pearce, J.A.; Thirlwall, M.F.; Mitchell, J.G. Petrogenetic evolution of late Cenozoic, post-collision volcanism in western Anatolia, Turkey. *J. Volcanol. Geotherm. Res.* **2000**, *102*, 67–95. [[CrossRef](#)]
98. Pearce, J.A.; Harris, N.B.W.; Tindle, A.G. Trace element discrimination diagrams for the tectonic interpretation of granitic rocks. *J. Pet.* **1984**, *25*, 956–983. [[CrossRef](#)]
99. Xia, L.-Q. The geochemical criteria to distinguish continental basalts from arc related ones. *Earth-Sci. Rev.* **2014**, *139*, 195–212. [[CrossRef](#)]
100. Wang, J.R.; Pan, Z.J.; Zhang, Q.; Chen, W.F.; Yang, J.; Jiao, S.T.; Wang, S.H. Intra-continental basalt data mining: The diversity of their constituents and the performance in basalt discrimination diagrams. *Acta Petrol. Sin.* **2016**, *32*, 1919–1933, (In Chinese with English Abstract)
101. Wang, X.C.; Wilde, S.A.; Xu, B.; Pang, C.J. Origin of arc-like continental basalts: Implications for deep-Earth fluid cycling and tectonic discrimination. *Lithos* **2016**, *261*, 5–45. [[CrossRef](#)]
102. Sobolev, A.A.; Hofmann, A.W.; Kuzmin, D.V.; Yaxley, G.M.; Arndt, N.; Ai, E. The amount of recycled crust in sources of mantle derived melts. *Science* **2007**, *316*, 412–417. [[CrossRef](#)] [[PubMed](#)]
103. Ivanov, A.V.; Litasov, K.D. The deep water cycle and flood basalt volcanism. *Int. Geol. Rev.* **2014**, *56*, 1–14. [[CrossRef](#)]
104. Jian, P.; Kröner, A.; Windley, B.F.; Shi, Y.R.; Zhang, W.; Zhang, L.Q.; Yang, W.R. Carboniferous and Cretaceous mafic-ultramafic massifs in Inner Mongolia (China): A SHRIMP zircon and geochemical study of the previously presumed integral “Hegenshan ophiolite”. *Lithos* **2012**, *142–143*, 48–66. [[CrossRef](#)]
105. Song, S.G.; Wang, M.M.; Xu, X.; Wang, C.; Niu, W.L.; Allen, M.B.; Su, L. Ophiolites in the Xing’an-Inner Mongolia accretionary belt of the CAOB: Implications for two cycles of seafloor spreading and accretionary orogenic events. *Tectonics* **2015**, *34*, 2221–2248. [[CrossRef](#)]
106. Zhang, Z.C.; Li, K.; Li, J.F.; Tang, W.H.; Chen, Y.; Luo, Z.W. Geochronology and geochemistry of the Eastern Erenhot ophiolitic complex: Implications for the tectonic evolution of the Inner Mongolia–Daxinganling Orogenic Belt. *J. Asian Earth Sci.* **2015**, *97*, 279–293. [[CrossRef](#)]
107. Huang, B.; Fu, D.; Li, S.C.; Ge, M.C.; Zhou, W.X. The age and tectonic implications of the Hegenshan ophiolite in Inner Mongolia. *Acta Petrol. Sin.* **2016**, *32*, 158–176, (In Chinese with English Abstract)

108. Yang, J.; Zhang, Z.; Chen, Y.; Yu, H.; Qian, X. Ages and origin of felsic rocks from the Eastern Erenhot ophiolitic complex, southeastern Central Asian Orogenic Belt, Inner Mongolia China. *J. Asian Earth Sci.* **2017**, *144*, 126–140. [[CrossRef](#)]
109. Li, Y.J.; Wang, G.H.; Santosh, M.; Wang, J.F.; Dong, P.P.; Li, H.Y. Supra-subduction zone ophiolites from Inner Mongolia, North China: Implications for the tectonic history of the southeastern Central Asian Orogenic Belt. *Gondwana Res.* **2018**, *59*, 126–143. [[CrossRef](#)]
110. Liu, J.F.; Li, J.Y.; Zhang, W.; Zhang, J.; Zhao, S.; Yin, D. Newly discovered late Devonian and early Carboniferous ophiolite fragments in the Diyanmiao mélangé in southeastern Inner Mongolia: Implications for the late Paleozoic tectonic evolution of the southeastern Central Asian Orogenic Belt. *Lithos* **2022**, *408–409*, 106566. [[CrossRef](#)]
111. Jian, P.; Liu, D.Y.; Kröner, A.; Windley, B.F.; Shi, Y.R.; Zhang, W.; Zhang, F.Q.; Miao, L.C.; Zhang, L.Q.; Tomurhuu, D. Evolution of a Permian intraoceanic arc–trench system in the Solonker suture zone, Central Asian Orogenic Belt, China and Mongolia. *Lithos* **2010**, *118*, 169–190. [[CrossRef](#)]
112. Shao, J.A.; Zhang, L.L.; Zhou, X.H.; Zhang, L.Q.; Tang, K.D. A further study on the ophiolite in Hegenshan, Inner Mongolia. *Acta Petrol. Sin.* **2019**, *35*, 2864–2872, (In Chinese with English Abstract) [[CrossRef](#)]
113. Zhang, Y.J.; Xu, B.; Tian, Y.J.; Wang, Z.W. The Late Paleozoic extending processes of Xing’an-Mongolia Orogenic Belt (XMOB): Evidence from Carboniferous-Permian sedimentary basin in northeast of Erenhot, Inner Mongolia. *Acta Petrol. Sin.* **2018**, *34*, 3083–3100, (In Chinese with English Abstract)
114. Xu, B.; Wang, Z.W.; Zhang, L.Y.; Wang, Z.H.; Yang, Z.Y.; He, Y. The Xing-Meng Intracontinent Orogenic Belt. *Acta Petrol. Sin.* **2018**, *34*, 2819–2844, (In Chinese with English Abstract).
115. Shervais, J.W. Ti-V plots and the petrogenesis of modern and ophiolitic lavas. *Earth Planet. Sci. Lett.* **1982**, *59*, 101–118. [[CrossRef](#)]
116. Pearce, J.A. A user’s guide to basalt discrimination diagrams. In *Trace Element Geochemistry of Volcanic Rocks: Applications for Massive Sulphide Exploration*; Wyman, D.A., Ed.; Short Course Notes; Geological Association of Canada: St. John’s, NL, Canada, 1996; pp. 79–113.

Disclaimer/Publisher’s Note: The statements, opinions and data contained in all publications are solely those of the individual author(s) and contributor(s) and not of MDPI and/or the editor(s). MDPI and/or the editor(s) disclaim responsibility for any injury to people or property resulting from any ideas, methods, instructions or products referred to in the content.